Temperature dependent anisotropy and asymmetry evolution of α-Ti in thermomechanical working: Characterization and modeling

H. Yang [a], H. Li [a]*, J. Ma [a], D. Wei [a], J. Chen [b], M.W. Fu [c]

[a] State Key Lab of Solidification Processing, School of Materials Science and Engineering, Northwestern Polytechnical University, Xi'an, 710072, China
[b] Department of Plasticity Technology, Shanghai Jiao Tong University, Shanghai 200030, China
[c] Department of Mechanical Engineering, The Hong Kong Polytechnic University, Hung Hom, Kowloon, Hong Kong, PR China
* Corresponding authors. Email: liheng@nwpu.edu.cn

ABSTRACT:

The strong anisotropy, asymmetry and distorted evolution in thermal-mechanical processing of metallic materials such as α-Ti make it difficult to reveal the deformation behaviors. In this research, a general characterization framework is established to determine the anisotropic and asymmetrical deformation behaviors of α-Ti materials under different thermal-mechanical loading conditions. The temperature dependent discontinuous constitutive approach is developed for modeling of the distorted evolution of plasticity. By taking the thin-walled α-Ti tube as a study case, the high temperature digital image correlation (HT-DIC) measurement approach and EBSD based physical experiment are employed to obtain the fundamental tension/compression properties and texture evolution of the alloy at different working temperatures. The viscoplastic self-consistent (VPSC) crystal plasticity based FE simulation is conducted to determine the temperature dependent anisotropic and asymmetrical deformation behaviors. A multi-objective optimization based calibration method is developed for calibration of the VPSC model parameters. An interpolation approach is employed to smoothly present the nonlinear evolution of yield loci with strain and temperature. By considering five main deformation mechanisms, viz., prismatic slip, basal slip, pyramidal <c+a> slip, {10-12}<10-1-1> tension twinning and {11-22}<11-2-3> compression twinning, the interactive relationships among flow stress, R-value, yield locus, deformation mechanism, texture evolution and working temperature are established and elaborated. T the related findings include: 1). α-Ti tube shows a significant anisotropy and asymmetry in terms of the distributions of flow stress, R-value and yield locus at 298K, but they are significantly reduced at elevated temperature; 2). The texture changes significantly with temperature in twinning activated deformation, but is insensitive to temperature in slip dominated deformation; 3). The activation of slip systems produces an initial T-C symmetry based on flow stress and R-value, and then the asymmetric evolution occurs due to the discrepant rotation of grains; 4).The activation of twinning also generates the significant anisotropy and asymmetry and leads to the remarkably irregular evolution of yield loci.

Keywords: Anisotropy and asymmetry; Deformation mechanism; α-Ti; Thermomechanical working, Modeling and characterization.

Highlights

- A general characterization framework is developed based on observation, measurement and modeling for determination of the anisotropy and asymmetry of plastic deformation of materials.

- Temperature dependent discontinuous constitutive framework is constructed for modeling of the distorted evolution of anisotropic and asymmetrical plasticity.

- α-Ti has the significant anisotropy and asymmetry at room temperature but significantly reduced at elevated temperature.

- The texture of α-Ti changes obviously with temperature in twinning activated deformation, but insensitive to temperature in slip dominated deformation.

- Activation of slip systems of α-Ti produces an initial T-C symmetry in terms of flow stress and R-value and followed by the asymmetric evolution for the discrepant rotation of grains.

1. Introduction

Due to its high strength, lightweight, good corrosion resistance and biocompatibility, thin-walled α-Ti materials have widely been used in aerospace, marine, energy, healthcare, consumer electronics clusters (Hama et al., 2017; Raemy et al., 2017). α-Ti materials have the hexagonal close-packed (HCP) crystal structure with a c/a ratio (height of hexagon/length of basal side) of 1.587. Due to its HCP structure and the c/a ratio different from the ideal value of 1.633, the plastic deformation of α-Ti materials is accommodated by a combination of slip and twinning. This gives rise to more complex mechanical responses and deformation mechanism than those of the conventional steels and aluminum alloys. While undergoing complex multi-pass thermal-mechanical processing, such as casting, extrusion, rolling, thin-walled α-Ti materials can produce different microstructures and textures and further exhibit anisotropy and tension-compression (T-C) asymmetry in terms of flow stresses and R-value (Panda et al., 2014; Sahoo et al., 2016). All of these have a significant effect on the subsequent forming processes including bending, drawing, hydroforming and hot stamping (Gatea et al., 2018; Nie et al., 2018; Singh et al., 2018; Venugopal et al., 2008). α-Ti materials with a low asymmetrical HCP crystal structure and various temperature dependent deformation mechanisms are easier to produce inhomogeneous deformation in thermal-mechanical fabrication processes (Orozco-Caballero et al., 2018; Xu et al., 2017). Along with the non-uniform deformation and temperature fields, diverse deformation modes could result in the preferred crystallographic reorientation and the texture evolution, which in turn escalate the inhomogeneous deformation, intensify anisotropy and asymmetry, further bring about plastic instability and fracture. Therefore, for integrated design and development of the forming process for making titanium products aiming at accurate forming of product geometry and desirable tailoring of the satisfied quality and properties, it is critically needed to establish a whole spectrum of knowledge of the anisotropy and asymmetry of deformation behaviors and deformation mechanisms of thin-walled α-Ti materials under complex thermal-mechanical loading conditions.

So far, many researches have been done to explore the plastic deformation behaviors, including flow stress, strain hardening and yield locus, and to reveal the underlying mechanisms under different thermal-mechanical loading conditions for α-Ti materials by using physical experiment, microstructure observation and atomistic/continuum modeling (Ahn et al., 2015; Bishoyi et al., 2017; Gurao et al., 2011; Rawat and Mitra, 2018; Wronski et al., 2018). The earlier studies are mainly concerned with the uniaxial tension/compression deformation behavior at different strain rates and temperatures (Chichili et al., 1998; Huang et al., 2007;

Nemat-Nasser et al., 1999; Zeng et al., 2009b; Zhang et al., 2013), and revealed that the flow stress, yield point and strain hardening of α-Ti are strongly dependent on strain rate and working temperature. The recent researches, however, indicate that α-Ti at room temperature also demonstrates pronounced anisotropic and asymmetrical yielding, as well as remarkable distorted evolution of plasticity (Baral et al., 2018; Nixon et al., 2010b; Williams and Boyle, 2016).

The deformation anisotropy of α-Ti materials is attributed to the HCP structure with crystal anisotropy (Hama et al., 2017; Li et al., 2017; Nixon et al., 2010a), and thus requires two types of deformation modes, slip and/or twinning (Gurao et al., 2011; Raemy et al., 2017; Suwas et al., 2011; Ungár et al., 2008). In particular, the primary slip system in α-Ti is prismatic slip <a>: {10-10}<11-20>; while basal slip <a>: {0001}<11-20> and pyramidal slip <a>:{10-11}<11-20> are also active (Hama et al., 2014; Warwick et al., 2012). Due to the fact that these three slip modes can only provide four independent slip systems, at least one other independent deformation mode is necessary to satisfy the von Mises criterion (Yoo, 1981). Based on the earlier studies, it is known that pyramidal slip <c+a>: {10-11}<11-23>, {11-22}<11-23>, {11-21}<11-23>, or twinning may act as an additional deformation mode (Hama et al., 2017; Liu et al., 2018; Orozco-Caballero et al., 2018; Zeng et al., 2009c). In addition, even if the pyramidal slip systems have a favorable orientation for activation throughout the entire deformation, pyramidal slip <a>:{10-11}<11-20> and pyramidal slip <c+a>: {11-22}<11-23> are rarely activated (Knezevic et al., 2013; Zeng et al., 2009c). The critical resolved shear stress (CRSS) are also different significantly depending on the family of slip systems (Qin et al., 2014). Specially for rolled α-Ti materials which usually possess strong basal texture, the activity of slip systems is very sensitive to loading direction (Hama et al., 2017, 2014; Yi et al., 2016), which could result in a significant anisotropic yielding.

Deformation twinning is a prevalent plastic deformation mode in HCP metals due to a lack of available and easily activated slip modes to accommodate irreversible deformation along the c-axis (Chichili et al., 1998; Hama et al., 2017; Nemat-Nasser et al., 1999; Zeng et al., 2009a; X. Zhang et al., 2014). The {10-12}<10-11> tensile twinning and {11-22}<11-2-3> compressive twinning are most frequently observed during plastic deformation of α-Ti materials (Gurao et al., 2011; Lin et al., 2017; Tirry et al., 2012; Yi et al., 2016). The {10-21}<11-2-6> tensile twinning and {10-11}<10-1-2> compressive twinning are difficult to be activated in α-Ti because of the high twinning shear strain and the large shuffling parameter, respectively (Chun et al., 2005). In addition, the activity of twinning systems significantly depends on the loading condition due to the direction dependence in deformation. For instance, in the rolled α-Ti sheets, {10-12}<10-11> and {10-21}<11-2-6> twins are formed when the loading condition extends the

crystal along the c-axis, {11-22}<11-2-3> and {10-11}<10-1-2> twins are formed when the loading condition results in the contraction of crystal along the c-axis (Hama et al., 2014; Yi et al., 2016; X. Zhang et al., 2014), resulting in a pronounced T-C asymmetry in yielding and plastic flow.

The above-reviewed studies provide abundant knowledge about the anisotropy and asymmetry of deformation behaviors and mechanisms of α-Ti materials at room temperature. Under elevated temperature, on the other hand, the available researches are mainly focused on uniaxial tension and compression deformation behaviors and mechanisms of α-Ti materials (Bishoyi et al., 2017; Nemat-Nasser et al., 1999; Tsao et al., 2012; Zeng et al., 2009b; Zhang et al., 2013). With the development of warm/hot forming technology and the wide application of thin-walled α-Ti materials (Djavanroodi and Janbakhsh, 2013; Karbasian and Tekkaya, 2010; Tekkaya et al., 2015), the temperature dependent anisotropy and asymmetry of deformation behaviors and mechanisms need to be explored.

For thin-walled materials, buckling is very easy to happen under uniaxial compression loading. To avoid it, researchers have developed many innovative methods, such as stack sheet compression tests (Ghaffari Tari et al., 2014; Martínez et al., 2017), compression with anti-instability devices (Bennett et al., 2010; Cao et al., 2009), small-cube compression test (Kitamura and Terano, 2014), compression using a small gauge-length sample (ul Hassan et al., 2016). However, for thin-walled tubular materials, due to geometry and property non-linearity, how to obtain anisotropic and asymmetrical mechanical properties is still a non-trivial issue and has attracted many attentions (Cui and Yuan, 2016; He et al., 2014, 2010; Jiang et al., 2008). Considering the visco-plastic self-consistent (VPSC) model with the capability of being able to predict the slip/twinning coordinated deformation, it is thus used in exploring the deformation behaviors of α-Ti materials (Gurao et al., 2011; Knezevic et al., 2013; Li et al., 2017; Wronski et al., 2018). While the reliability of VPSC-based computation is strongly dependent on the robust calibration of the mesoscale parameters of crystal plasticity. For α-Ti materials, model parameter identification is difficult due to the large number of active deformation modes (Hama et al., 2017). Therefore, a general characterization method needs to be developed for determination of the temperature related anisotropy and asymmetry of plastic deformation for thin-walled α-Ti.

To understand the unique plastic anisotropy and asymmetry, the constitutive modeling of materials is an efficient approach (Banabic, 2010; Lee and Barlat, 2014; Smith et al., 2015). Developing the constitutive formulations at macroscopic level is a preferable way to achieve accurate and efficient modeling and simulation of complex forming of α-Ti materials under thermal-mechanical loading conditions. To characterize the texture-induced anisotropy, many

anisotropic models such as Hill'48, YLD2004-18p, Banabic model (Banabic, 2010; Barlat et al., 2005; Hill, 1948) have been proposed. In addition, some efforts have been made to describe the yield asymmetry aside from plastic anisotropy (Cazacu et al., 2006; Plunkett et al., 2008; Tuninetti et al., 2015; Yoon et al., 2014). Taking the combined isotropic, kinematic and distortional hardening into account, Shutov and Ihlemann proposed a rheological model to describe the distorted evolution of the yield surface for an annealed aluminum alloy (Shutov and Ihlemann, 2012). By using the interpolation approach, Li et al., constructed a unified continuum-based discontinuous framework to capture the distorted shape of the yielding and its nonlinear evolution in the full stress space (Li et al., 2016). Until now, modeling the distorted plasticity and its evolution with strain and temperature in the full stress space still remains a challenge in metal forming arena.

In this research, as shown in Fig. 1, a general characterization framework is developed to determine the anisotropic and asymmetrical plastic behaviors of α-Ti materials. In this research framework, the high temperature digital image correlation (HT-DIC) and EBSD based physical experiment are firstly conducted to determine the fundamental mechanical properties and texture evolution under tension and compression deformation of thin-walled α-Ti tube. The viscoplastic self-consistent (VPSC) crystal plasticity based modeling is then conducted to determine the

6
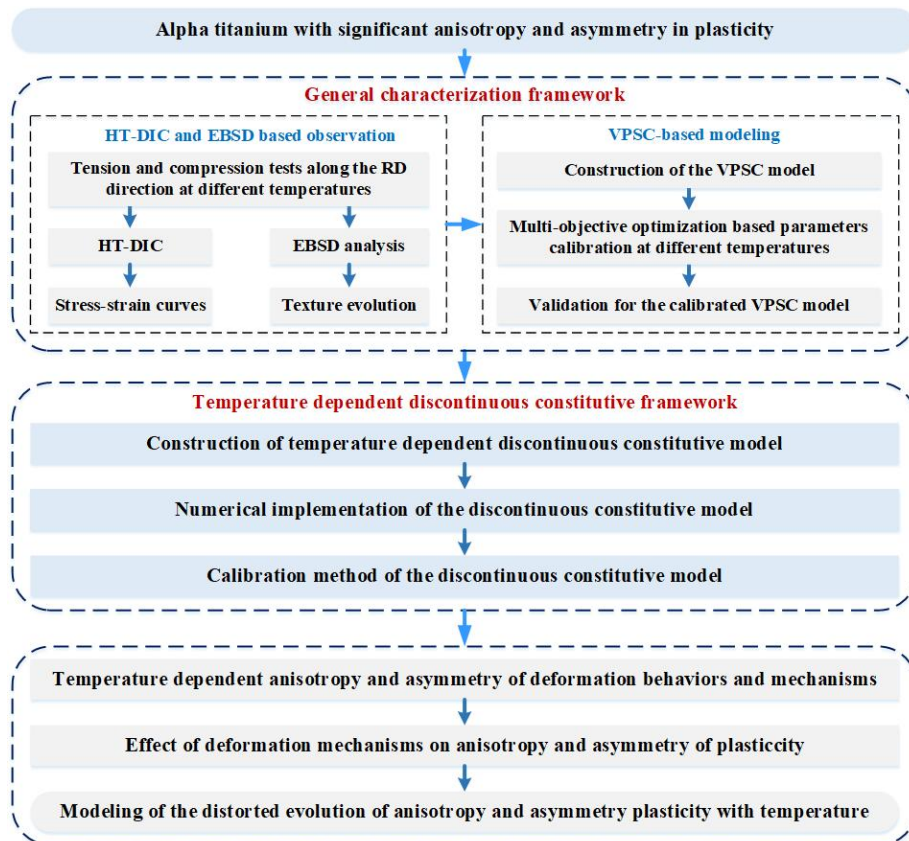
Fig. 1. A general characterization and modeling framework for α-Ti materials.

temperature dependent anisotropy/asymmetry of plastic deformation of α-Ti tube. By using an interpolation approach to smoothly representing the nonlinear evolution of the distorted plasticity with strain and temperature in the full stress space, the temperature dependent discontinuous constitutive framework is constructed and numerically implemented. Finally, the effects of temperature on the anisotropy and asymmetry in terms of flow stress, R-value, deformation mechanism, texture evolution and yield locus are elaborated, and the mechanism of plastic anisotropy and asymmetry is clarified.

2. A general characterization framework

By combining HT-DIC and EBSD based observation techniques with VPSC-based modeling method, a general characterization framework is proposed to determine the temperature dependent anisotropic and asymmetrical plasticity of α-Ti materials in thermomechanical working process.

2.1 HT-DIC and EBSD based observation and experiment

The HT-DIC system and the designed uniaxial tension/compression specimens are employed to obtain the stress-strain curves of α-Ti during tension/compression deformation at various temperatures and the micro texture and its evolution are determined by EBSD analysis.

2.1.1 As-received materials

The as-received material of α-Ti is the commercially pure titanium welded tube with the dimension of 76.2mm×1.07mm (tube diameter × wall thickness) following the standard of SAE AMS4941E. The chemical composition is given in Table 1. The α-Ti tube is commonly used for making parts for different applications such as low-pressure fluid-conducting lines and conduits. The welded zone is relatively small and can be placed at the place with a small plastic deformation such as the neutral position of tube bending in such a way to have a little effect on the bending formability (Z. Zhang et al., 2014).

Table 1 The chemical composition of the tube (SAE, 2010).

Element	C	O	Fe	N	H	Other elements	Ti
Max. content (%)	0.10	0.25	0.20	0.05	0.015	0.15	remainder

The initial microstructure and texture of α-Ti tube are shown in Fig. 2(a) and (b), respectively. The as-received α-Ti has equiaxed grains with an average grain size of 15 μm. The initial texture shows a bimodal distribution and the maximum intensity of 6.27 exists in the locations of 45° from the normal direction (ND) to the transverse direction (TD).
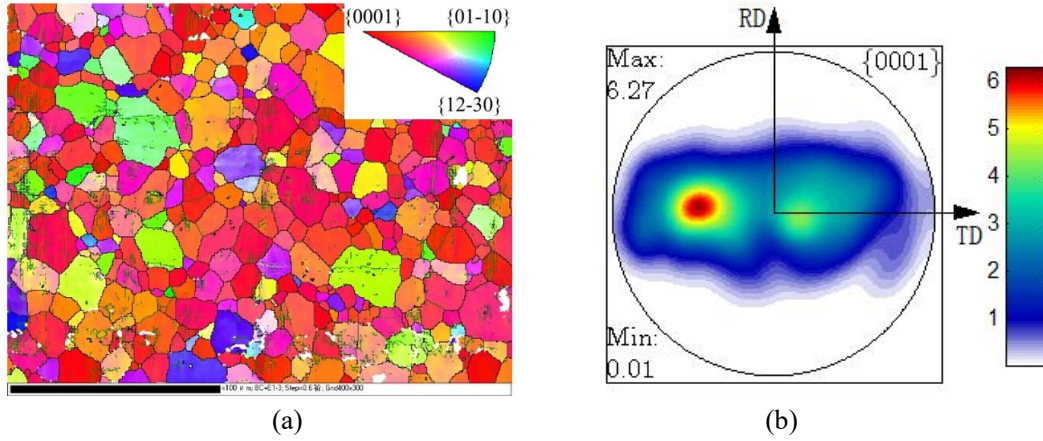
**Fig. 2.** Initial (a) microstructure and (b) texture of the α-Ti tube.
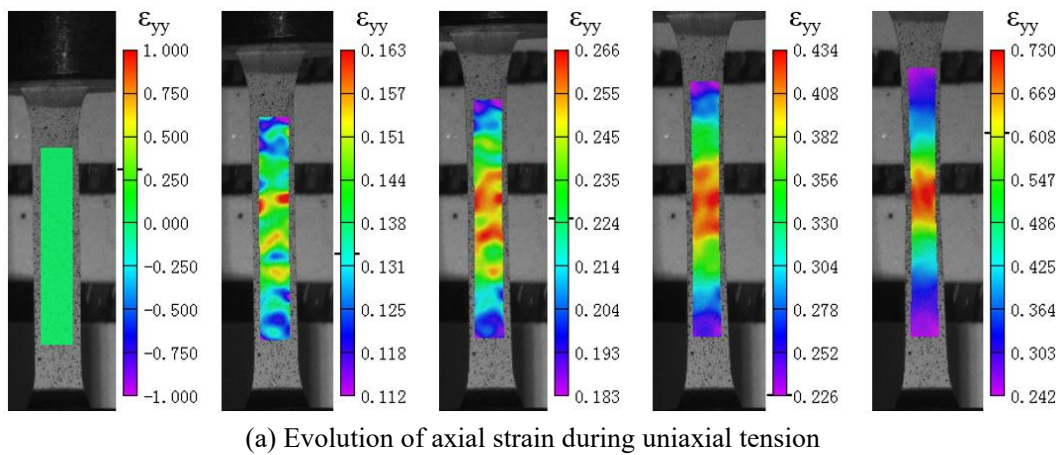
2.1.2 HT-DIC based uniaxial tension and compression

The arc tube tensile specimens are designed and directly cut along the rolling direction (RD) of α-Ti tube, as shown in Fig. 3(a). To avoid the buckling under uniaxial compression loading, the small-column samples, as shown in Fig. 3(a), are designed and cut along the RD. The quasi-static tensile and compressive tests are carried out on an electronic universal testing machine with HT-DIC measuring system, as shown in Fig. 3(b). The force shifting device is designed to transform the tension to the compression. For the small-column compression test, the compressive strain is determined by measuring the distance between up and down dies. The experiments are carried out at 298, 423 and 573K with the nominal strain rate of 0.001s⁻¹. Under a constant temperature, the specimens are stretched to failure. The compression tests are stopped when the displacement is up to 1.2mm. To get a homogenous temperature distribution, three thermocouples are attached to the top side, central part and down side of the samples, respectively.

The axial strain evolution measured by the HT-DIC system is shown in Fig. 4(a). It is found that the strain inhomogeneity is increased with tension deformation. Fig. 4(b) shows the axial displacement variation of the up and down dies in compression, which is used to determine the compression strain of the small column samples. Fig. 5(a) shows the nominal stress-strain curves of α-Ti tube during tension and compression deformation at different temperatures. At room temperature, although there is no significant difference in yielding behavior, the T-C
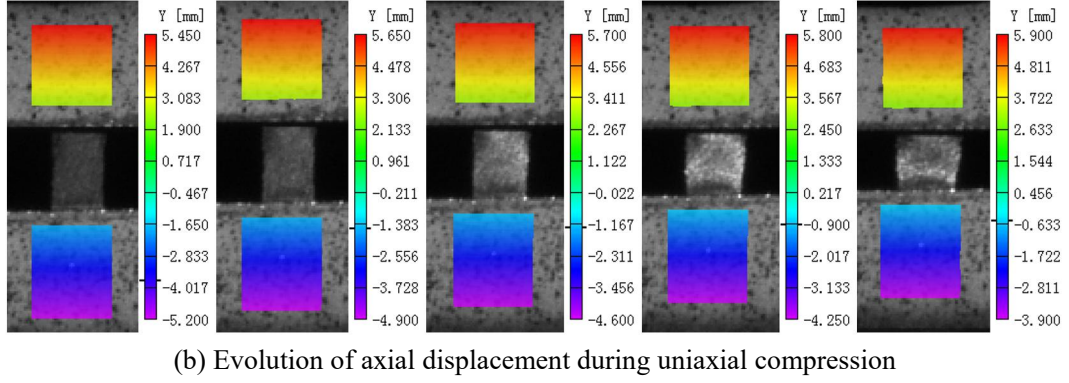
asymmetry is remarkably increased with deformation. Similar observations are reported by peers (Baral et al., 2018; Nixon et al., 2010a; Wronski et al., 2018; Zhai et al., 2016). With the increase of temperature, the T-C asymmetry tends to decrease. The true stress-plastic strain curves are obtained by fitting the true stress-logarithmic strain curves using Swift hardening law. From Fig. 5(b), with the increasing working temperature, the T-C asymmetry is significantly reduced and an approximate T-C symmetry is observed at 523K. The change of flow stress reveals the decrease of twinning activation. This assumption will be validated by the observation of the textures in the deformed specimen in the subsequent sections.

(a)   (b)
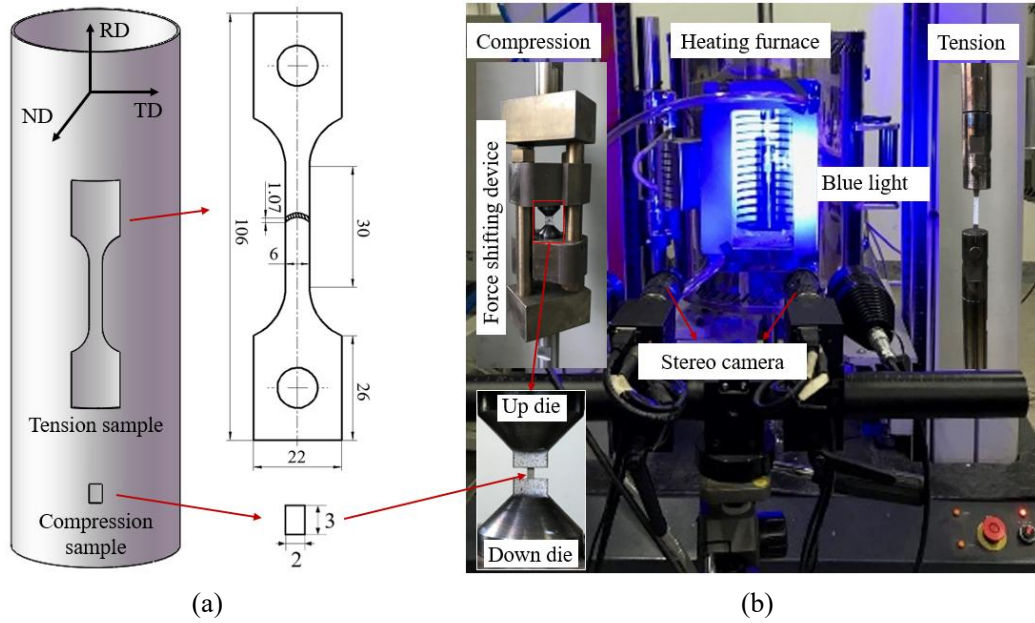
Fig. 3.   Experiment set-up: (a) tension and compression samples and (b) HT-DIC testing system.

(a) Evolution of axial strain during uniaxial tension

(b) Evolution of axial displacement during uniaxial compression

Fig. 4. Contours of axial strain and displacement obtained with HT-DIC system.

(a) Nominal stress-strain curves

(b) True stress-plastic strain curves
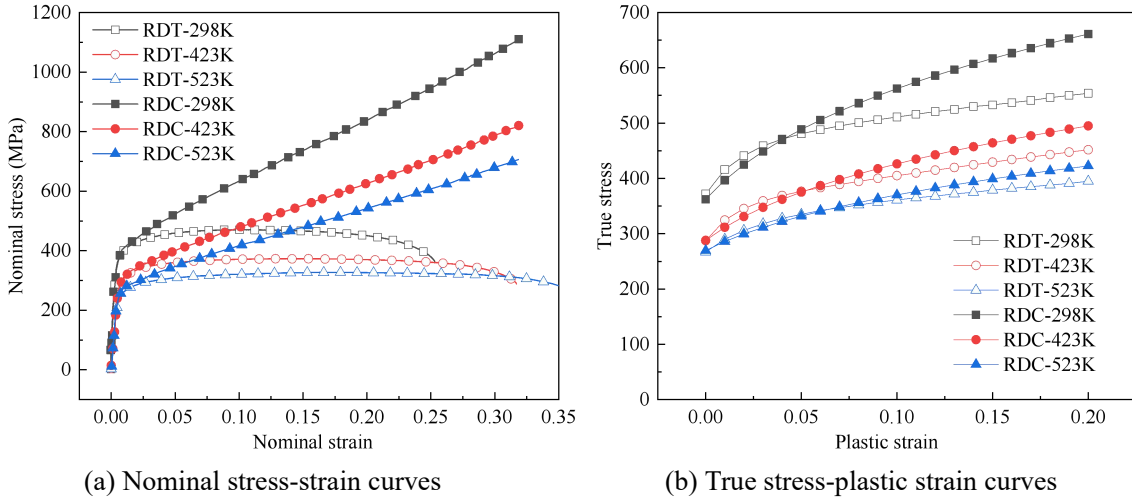
Fig. 5. Comparison between the tension and compression response at various temperatures.
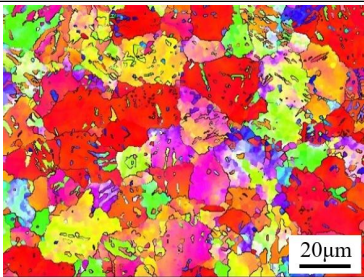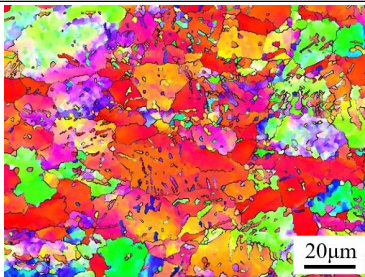
2.1.3 Micro texture and its evolution in tension and compression by EBSD
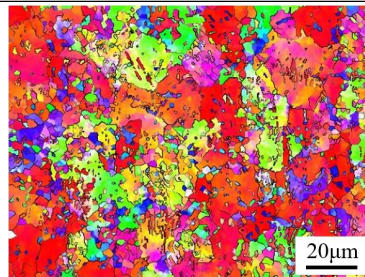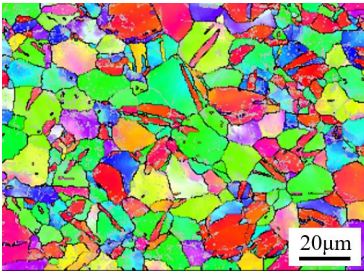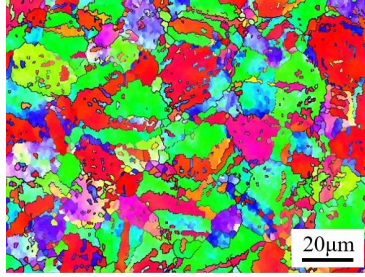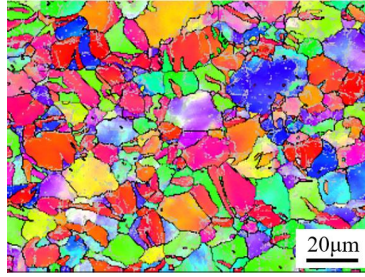
The metallographic micro texture of α-Ti tube and its evolution in tension/compression deformation are quantified using SEM-EBSD method. The scanning area of each color map is 50×50 mm with a step size of 0.1 mm in a MIRA3XMU equipped with an HKL EBSD system. The EBSD data is acquired and processed with the Channel 5 software to get the pole figures of the as-received material. The EBSD samples are prepared by wire cutting, grinding, mechanical polishing and electro-polishing. For the tension/compression tests at various temperature, different samples are strained to 20% for characterization purpose. As the deformation temperature is below the transformation temperature (1157K), the possible influence of beta phase on the deformation behavior can be eliminated.
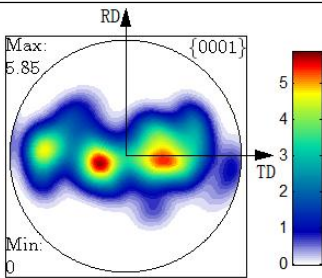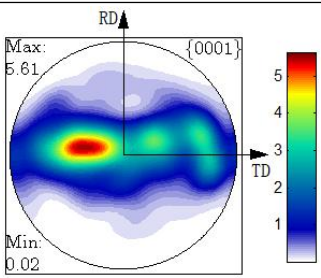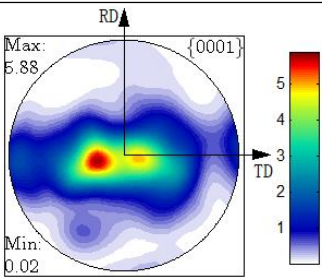
The EBSD maps of α-Ti tube with an approximate plastic strain of 0.2 at different temperatures are shown in Table 2. It is found that the grain orientation changes little in tension but much in compression. Table 3 shows the (0001) pole figures of the deformed samples at different temperatures. In addition, the c-axes of the HCP crystals change slightly in tensile
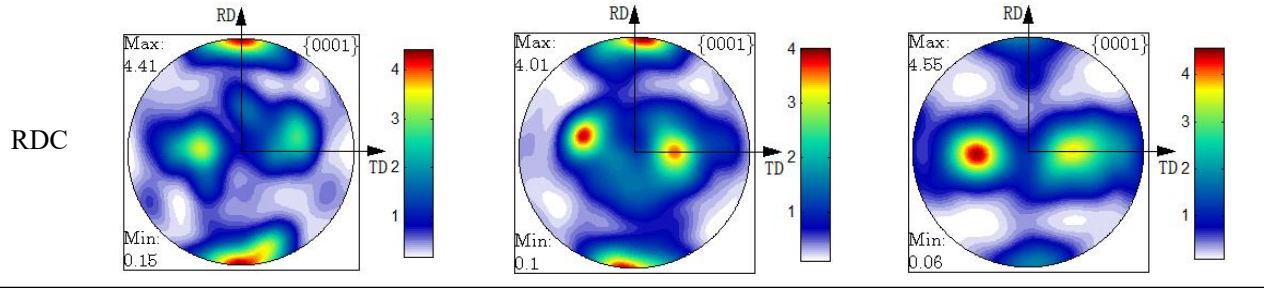
deformation at different temperatures, and the textures still present with a bimodal distribution. For the compressive deformation at different temperatures, however, the c-axes reorientate toward the RD, and the textures turn into the coexisting states of both the rolling texture (<0001>//RD) and the bimodal texture. At room temperature, the intensity of the rolling texture is larger than that of the bimodal texture. With the increase of temperature increasing, the intensity of the rolling texture is decreased gradually and is less than that of the bimodal texture at 523K. The main reason is the activity of twins is decreased with the increase of temperature (Bishoyi et al., 2017). The detailed analysis will be elaborated in the subsequent section.

Table 2 Microstructure of α-Ti tube after 20% tension/compression deformation along the RD.

**Table 3** Texture of α-Ti tube after 20% tension/compression deformation along the RD.

RDC

Figs. 6 (a) and (b) show the change of volume fraction of the grains with softer orientation at different temperatures for prismatic slip <a>: {10-10}<11-20> (Pr); basal slip <a>: {0001}<11-20> (Ba) and pyramidal slip <c+a>: {10-11}<11-23> (Py), which are considered in the VPSC model for α-Ti materials (Gurao et al., 2011; Suwas et al., 2011; Wronski et al., 2018). The softer orientation refers the Schmid factor with larger than 0.25. It seems that, for Pr, Ba and Py slip modes, more than 40% of the grains remain softer orientation in tension or compression. It is thus reasonable to consider the Pr, Ba and Py slip modes in the VPSC modeling of as-received α-Ti tube.

To determine the twinning activity in plastic deformation of α-Ti tube, the volume fractions of twins are determined in tension and compression by EBSD, as shown in Figs. 6(c) and (d). It is found that the volume fractions of {10-12}<10-11> tensile twinning are more than 3% in tension and 12% in compression, and thus this twinning can be thought as one of the dominated twinning mechanisms. In addition, {11-22}<11-2-3> compressive twinning can be activated slightly, and the activity of {10-21}<11-2-6> and {10-11}<10-1-2> twins can be negligible. Accordingly, both the tensile twinning {10-12}<10-11> (Tt) and the compressive twinning {11-22}<11-2-3> (Ct) can be regarded as the dominant twinning modes in plastic deformation of α-Ti tube. The identification of these deformation mechanisms lays a basis for the VPSC-based simulation.
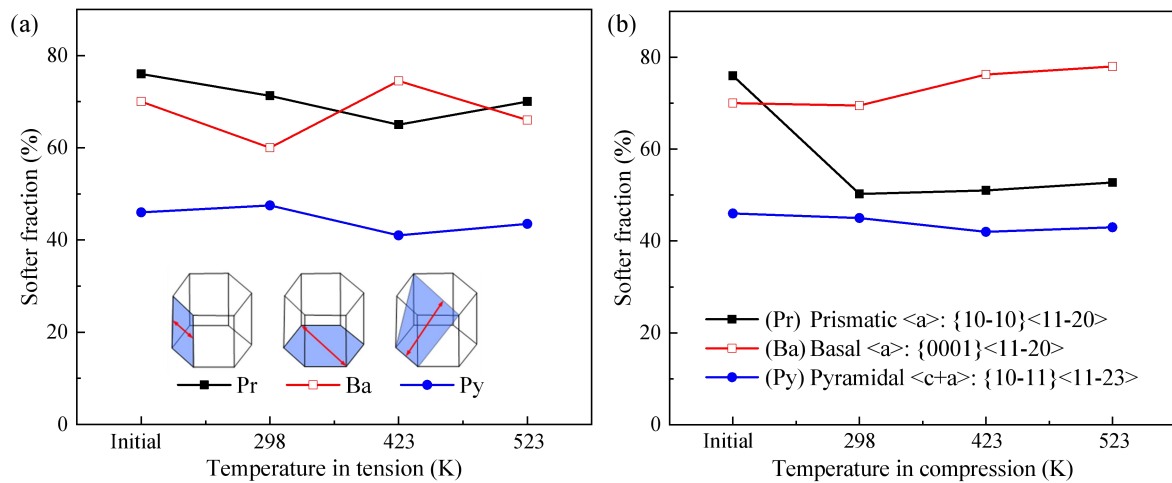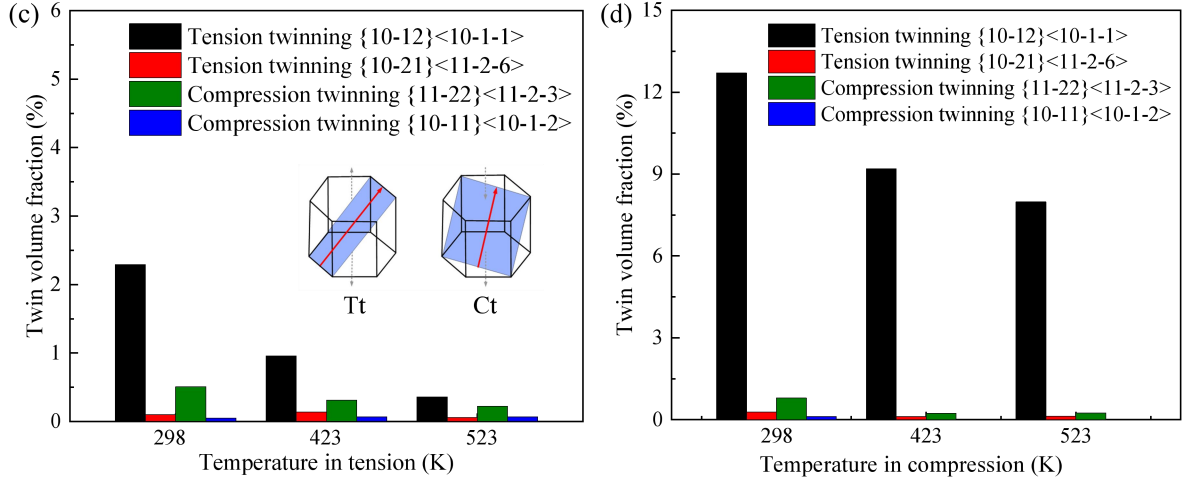
Fig. 6.   Evolution of slipping and twinning: volume fraction of the grains with softer orientation in (a) tension and (b) compression; twin volume fraction in (c) tension and (d) compression.

2.2 VPSC based virtual experiment

To study the anisotropy/asymmetry behaviors and underlying deformation mechanisms of α-Ti materials, the visco-plastic self-consistent (VPSC) crystal plasticity modeling is employed. A multi-objective optimization based calibration method is proposed for determining the VPSC model parameters. The VPSC model is validated by the R-values in uniaxial tension/compression and the texture evolution in mandrel bending.

2.2.1 VPSC model of the thin-walled α-Ti

Macroscopic responses of the α-Ti tube are simulated using the VPSC crystal plasticity model. VPSC model models the polycrystal as a collection of grains with the associated volume fractions chosen to represent the initial texture of the aggregate. Each grain can be treated as an anisotropic visco-plastic ellipsoidal inclusion embedded in a homogenous effective medium. The plastic deformation of each individual grain is assumed to occur by slip and/or twinning depending on the grain orientation, grain shape and the interaction with the effective medium. A comprehensive description of the VPSC model can be found in the previous research (Li et al., 2017). Only the hardening formulas and the twinning model are briefly presented in the following.

For individual deformation system including slip and twinning, an extended Voce hardening law, as designated in Eq. (1), is employed to describe the evolution of the threshold stress with the accumulated shear strain in each grain.

$$\tau^s = \tau_0^s + \left(\tau_1^s + \theta_1^s \Gamma\right)\left[1 - \exp\left(-\theta_0^s \Gamma \middle/ \tau_1^s\right)\right] \tag{1}$$

where τ^s is the instantaneous CRSS, $\Gamma = \sum_s \Delta\gamma^s$ is the accumulated shear in the grain, τ_0^s and $\tau_0^s + \tau_1^s$ are the initial CRSS and the final back-extrapolated CRSS, θ_0^s and θ_1^s are the initial hardening rate and the asymptotic hardening rate, respectively.

The model takes into account the possibility of 'self' and 'latent' hardening by introducing the coupling coefficient $h^{ss'}$ empirically considering the obstacles that new dislocations associated with s' activity represent for the propagation of system s. The increase in the threshold stress of a system due to shear activity $\Delta\gamma^{s'}$ in the grain systems is calculated as:

$$\Delta\tau^s = \frac{d\tau^s}{d\Gamma}\sum h^{ss'}\Delta\gamma^{s'} \tag{2}$$

where $\Delta\tau^s$ is the increase of the CRSS of a slip system due to shear activity.

The contribution of twinning reorientation to the texture evolution can be modeled by the predominant twin reorientation scheme (PTR) (Tomé et al., 1991). For the PTR scheme, within each grain g, both the shear strain $\gamma^{t,g}$ contributed by each twin system t and the associated volume fraction $V^{t,g} = \gamma^{t,g}/S^t$ are recorded, and S^t is the characteristic twin shear. The sum over all the twin systems of a given mode and over all the grains represents the accumulated twin fraction $V^{acc,mode}$ in the aggregate for the particular twin mode:

$$V^{acc,mode} = \sum_g \sum_t \frac{\gamma^{t,g}}{S^t} \tag{3}$$

Since it is not numerically feasible nor physically justifiable to regard each twinned fraction as an independent new grain, the PTR scheme adopts a statistical approach, viz., at each increment, some grains are fully reoriented by twinning provided that the accumulated twin fraction is larger than the so-called threshold volume fraction V^{th}, as denoted in the following:

$$V^{th} = A^{th1} + A^{th2}\frac{V^{eff}}{V^{acc}} \tag{4}$$

where V^{eff} is the effective twinned fraction represented by these fully reoriented grains for each of the twin modes. After each deformation increment, a grain at random is selected and the twin system with the highest accumulated volume fraction is identified. If the latter is larger than the threshold V^{th}, the grain is then allowed to reorient and V^{eff} and V^{th} are updated. The process is repeated until either all the grains are randomly checked or until the effective twin volume exceeds the accumulated twin volume. A total of 6,155 crystal orientations from the

EBSD result are directly used in the VPSC modeling to explore the temperature dependent anisotropy/asymmetry behaviors and underlying deformation mechanisms of α-Ti tube.

2.2.2 Parameter calibration for the established VPSC model

One of the most non-trivial tasks in the VPSC-based computation is to determine the accurate parameter values for generating the best simulation results, whilst still being realistic and well constrained. According to the used Voce hardening and latent hardening, a total of nine types of parameters should be calibrated, viz., Voce hardening related parameters τ_0^s, τ_1^s, θ_0^s, θ_1^s; and latent hardening related parameters h_s^{Pr}, h_s^{Ba}, h_s^{Py}, h_s^{Tt}, h_s^{Ct}. In addition, for the two twinning mechanisms, three kinds of PTR scheme related parameters, viz., twin shear S, A^{th1} and A^{th2}, should be determined. Both S^{Tt} and S^{Ct} are assigned as 0.167 and 0.225, respectively; A^{th1} and A^{th2} are given by 0.1 and 0.5, respectively. For the as-received α-Ti tube, three slipping systems (Pr, Ba and Py) and two twinning modes (Tt and Ct) are the dominant mechanisms, so that there are a total of 45 parameters for the VPSC model of α-Ti tube.

The initial values and reference ranges of the hardening parameters for the above-mentioned mechanisms are determined based on the previous reports (Gurao et al., 2011; Knezevic et al., 2013; Wronski et al., 2018). The optimized parameters are determined by minimizing the difference between the experimental data and the simulated ones. The flow stress, R-value, texture evolution and twin volume fraction evolution during plastic deformation can all be used as the optimization objective. In this section, the hardening parameters at room temperature are determined firstly. The experimental data at the elevated temperatures is then fitted by reducing the values of the hardening parameters. The twinning is believed to be less temperature sensitive (Chichili et al., 1998; Zhou et al., 2016), so the values of the hardening parameters for twinning remain nearly constant, while the values for thermally activated slips are decreased with the increase of temperature (Williams et al., 2002; Zeng et al., 2009b).

In addition, it should be noted that the insufficiency of the optimization targets would lead to the multi-solution problem. More optimization objectives can ensure more accurate parameters to be obtained, but require more time-consuming. To avoid the multi-solution problem and reduce the time consumption of the calibration process, a multi-objective optimization based calibration method considering both flow stress and texture evolution during uniaxial tension and compression deformation is proposed to determine the parameters set for ensuring the validity of the crystal plasticity modeling. Taking the determination of the model parameters at

room temperature as an example, the multi-solution problem and the multi-objective optimization based calibration method are discussed as follows.

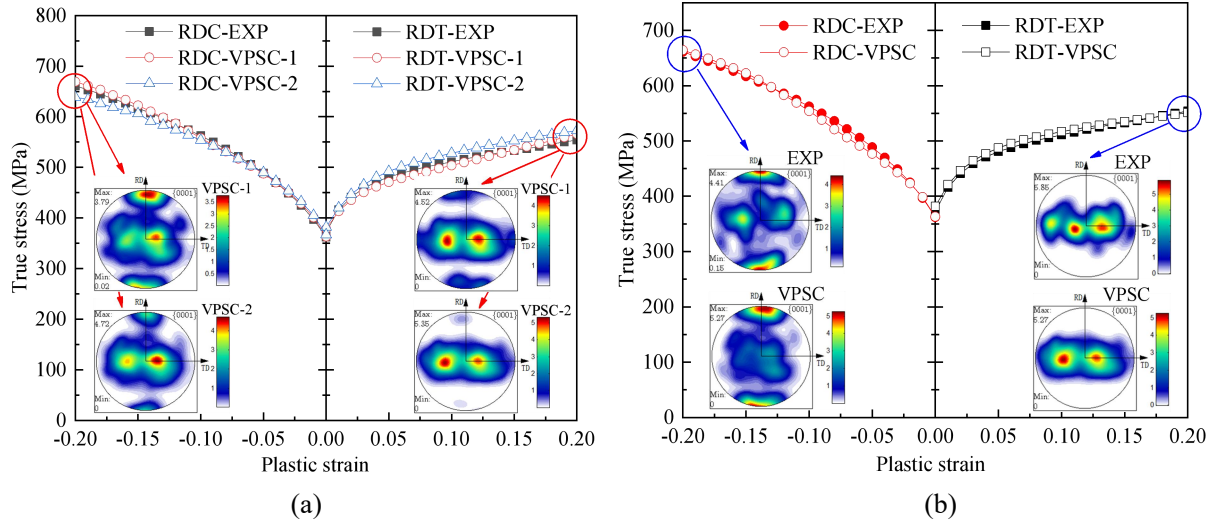- Flow stress single object optimization based calibration

The model parameters are determined by fitting the simulated hardening curve to the experimental one. From Fig. 7(a), when only the stress-strain curve under uniaxial tension along the rolling direction (RDT) is adopted as the optimization target, the predicted stress-strain curve under uniaxial compression along the rolling direction (RDC) differs greatly from the experimental results. When only the stress-strain curve under the RDC is adopted, the calibrated VPSC model also cannot reproduce the experimental result under RDT, as shown in Fig. 7(b). Accordingly, it is obvious that the parameters sets based on the single object optimization cannot model and capture the asymmetrical hardening behaviors of α-Ti tube well.
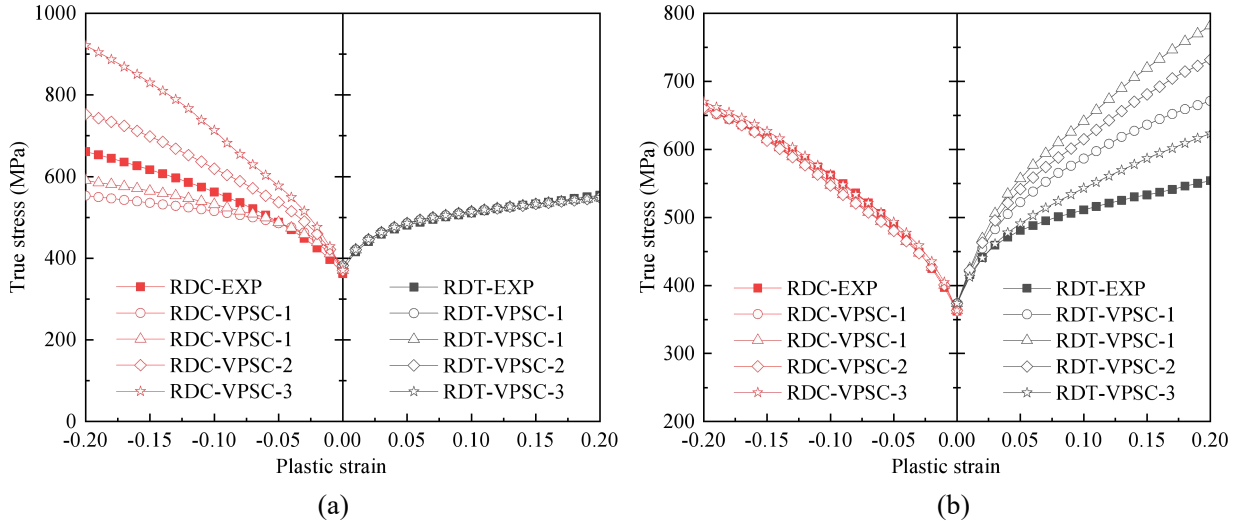
Fig. 7. Comparison of the experimental and the prediction results: (a) tension-based optimiztion; (b) compression-based optimization.

- Tension/compression flow stress double objects optimization based calibration

In the double objects optimization, through simultaneous fitting of both tensile and compressive stress-strain curves, the asymmetrical hardening behaviors can be represented accurately. However, from Fig. 8(a), there are different parameters sets that can satisfy the optimization targets. The predicted (0001) pole figures during uniaxial tension and compression cannot match the experimental ones well. Therefore, to further narrow the scope of the solutions of the model parameters, more optimization objectives should be introduced in the calibration method.

16

Fig. 8. Comparison of the experimental and the predicted results: (a) the double objects optimization; (b) the multi-objects optimization.

● Multi-object optimization based calibration

The stress-strain curves and the texture evolution during uniaxial tension and compression deformation are all introduced as the optimization targets for ensuring the validity of the VPSC model parameters. As shown in Fig. 8(b), the predicted stress-strain curves and (0001) pole figures in uniaxial tension and compression agree well with the experimental ones. It should be noted that, despite the discrepancy in texture density to some extent, the main features of texture reorientation during uniaxial tension and compression are accurately captured. Accordingly, the multi-object optimization based calibration method can be used to determine the best parameters set and avoid the multi-solution problem in the VPSC-based computation.

At the temperature of 423 and 523K, by reducing the values of the hardening parameters, the calculated stress-strain curves and pole figures are adjusted to match with the experimental ones. As shown in Fig. 9, the key features of texture reorientation during uniaxial tension and compression at 423 and 523K are accurately reproduced. That is, the textures show a bimodal distribution and the density distribution changes slightly during tensile deformation at different temperatures. Upon compression, the c-axes reorientate toward the RD, and the textures turn into the coexisting states of both the rolling texture (<0001>//RD) and the bimodal texture.
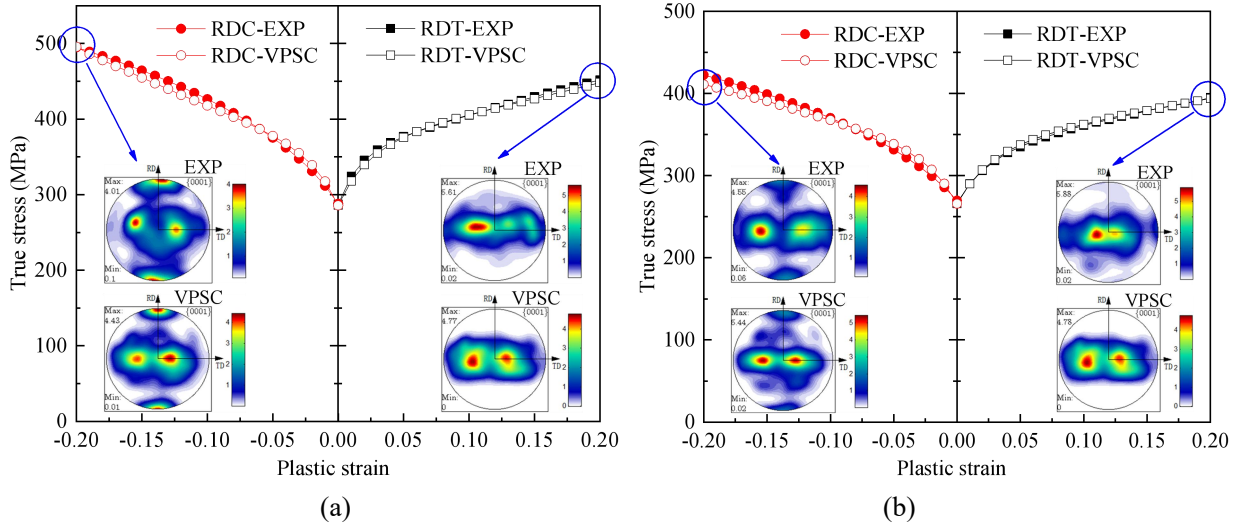
Fig. 9. Comparison of the experimental and the prediction results at (a) 423K and (b) 523K.

2.2.3 Validation of the established VPSC model

Tables 4, 5 and 6 show the finally obtained parameters of the VPSC model of α-Ti tube at the temperature of 298, 423 and 523K. Regarding the R-values in uniaxial tension/compression tests and the texture evolution in heat rotary draw bending (HRDB) with inhomogeneous deformation, the calibrated VPSC crystal plasticity model is thoroughly validated.

Based on the full-field strain data captured by HT-DIC system, the evolution of R-values (Lankford coefficients) can be determined for α-Ti tube in tension along the RD at different temperatures. The R-value can characterize the anisotropy and asymmetry of plastic flow and is defined as the ratio of the width-to-thickness plastic strain. The plastic strains are computed by subtracting the total strains with the elastic ones, which are determined by Hooke's law. Fig. 10 shows that the R-values are not constant, but first decrease and then stabilize with the increase of strain. With the increase of temperature, the R-values are decreased. This indicates there is no negligible evolution of the anisotropic plasticity of α-Ti tube.

Table 4 Parameters for the VPSC model of α-Ti tube at 298K.

|	τ_0	τ_1	θ_0	θ_1	h_s^{Pr}	h_s^{Ba}	h_s^{Py}	h_s^{Tt}	h_s^{Ct}
Pr	100	50	1200	60	1	1	1	3	10
Ba	235	30	800	80	1	1	1	3	10
Py	265	100	800	80	1	1	1	3	10
Tt	260	10	80	20	5	5	5	20	20
Ct	360	80	800	100	5	5	5	20	20

Table 5   Parameters of the VPSC model of α-Ti tube at 423K.

	τ_0	τ_1	θ_0	θ_1	h_s^{Pr}	h_s^{Ba}	h_s^{Py}	h_s^{Tt}	h_s^{Ct}
Pr	70	45	1000	100	1	1	1	3	10
Ba	150	30	900	80	1	1	1	3	10
Py	170	60	700	60	1	1	1	3	10
Tt	260	10	80	20	2	2	2	20	20
Ct	360	80	800	100	2	2	2	20	20

Table 6   Parameters of the VPSC model of α-Ti tube at 523K.

	τ_0	τ_1	θ_0	θ_1	h_s^{Pr}	h_s^{Ba}	h_s^{Py}	h_s^{Tt}	h_s^{Ct}
Pr	60	40	800	90	1	1	1	3	10
Ba	135	30	400	30	1	1	1	3	10
Py	160	50	400	20	1	1	1	3	10
Tt	260	10	80	20	1	1	1	20	20
Ct	360	80	800	100	1	1	1	20	20

By employing the calibrated VPSC model, the R-values at different temperatures are calculated and compared with the experimental ones, as shown in Fig. 10. At the lower levels of deformation, the predicted R-values differ greatly from the experimental ones. The main reason is that the experimental R-values are affected by elastic deformation, while the elastic effects are not considered in the VPSC-based computation. At the higher levels of deformation, the predicted R-values agree well with the experimental ones. Consequently, the calibrated VPSC models are reliable and can be used for determining the deformation behaviors of α-Ti tube.
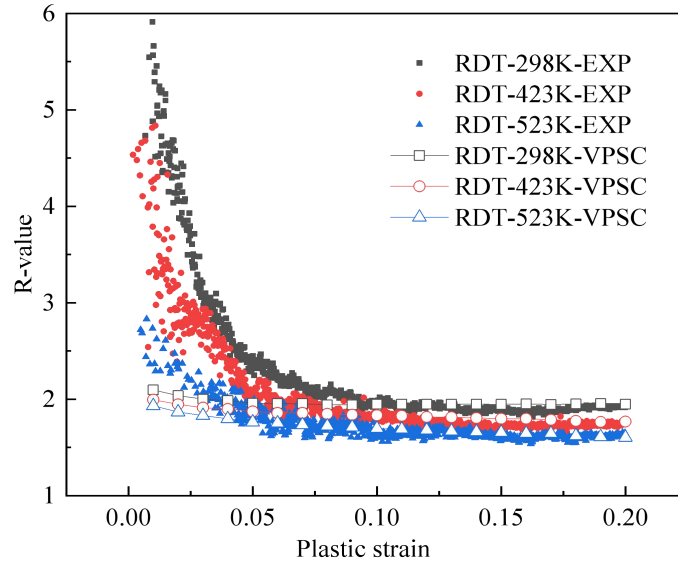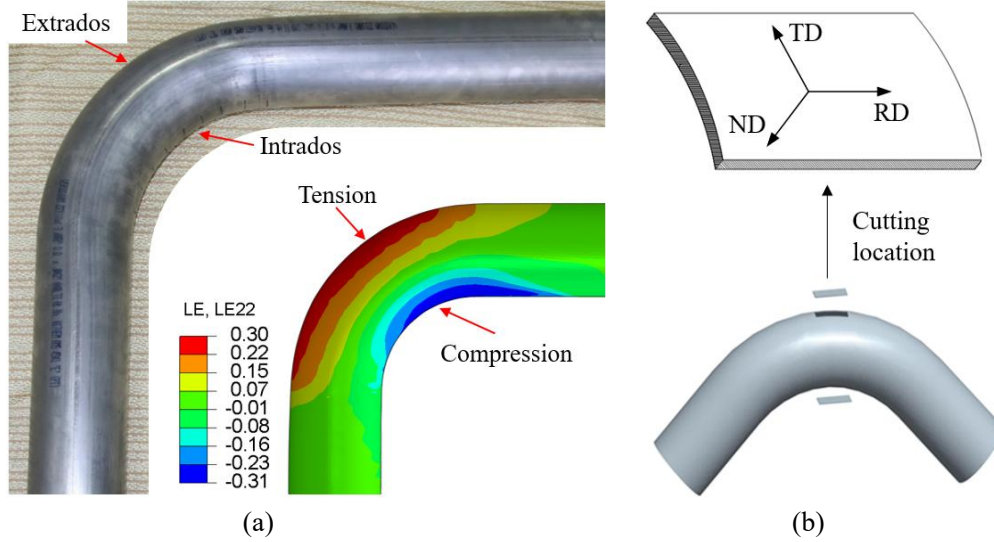
Fig. 10. Comparison of the experimental and predicted R-values in RDT.

For the HRDB of α-Ti tube, as shown in Fig. 11, the bending radius is 2.0 times the tube diameter, the bending angle is 90°, and the bending velocity is 1°/s. The HRDB is performed at 293, 423 and 523K, respectively. The detailed description of the FE models of the HRDB is given in the literature (Z. Zhang et al., 2014). The Mises yield criterion combined with Swift hardening law is employed for represnetation of the deformation behaviors of α-Ti tube. Upon bending, tensile stress and compressive stress will occur at the extrados and intrados of tube simultaneously (Li et al., 2018). Both the tension and compression strain at the extrados and intrados of the tube are larger and more inhomogeneous than those in uniaxial tension and compression. That is, the stress state in the HRDB is much complex than those in uniaxial tension and uniaxial compression. In the VPSC-based computation of the HRDB, the variable velocity gradient throughout the whole bending process is assigned into the VPSC models.

Using the combination of the VPSC model and the FE model, the texture evolution of α-Ti tube along bending at different temperatures is captured and shown in Table 7. It can be seen that, except for the minor difference in intensity, the predicted results can well reproduce the evolution features of the textures during tube bending at various temperature, viz., the c-axes of grains change slightly at the extrados of tube, and the c-axes of grains reorientate toward the RD at the intrados of tubes. It is thus sure that the calibration of the VPSC crystal plasticity model is valid and reliable. Accurate prediction of the flow stress, R-value, and texture evolution during different thermal-mechanical loading conditions indicates that the change of the relative activities of the slip and twin modes with temperature are reasonable.

Fig. 11. Schematic of (a) the T-C asymmetry in the HRDB and (b) the measuring locations of pole figures.

Table 7 Comparison of the experimental textures and the predicted ones for α-Ti tube.

3. Temperature dependent discontinuous constitutive framework

In the previous study (Li et al., 2016), a unified continuum-based discontinuous framework is proposed to model the distorted plasticity and its evolution of hard-to-deform materials in the full stress space. Based on this, the temperature dependent discontinuous constitutive framework is constructed for modeling of the anisotropic and asymmetrical plasticity and its evolution with strain and temperature.
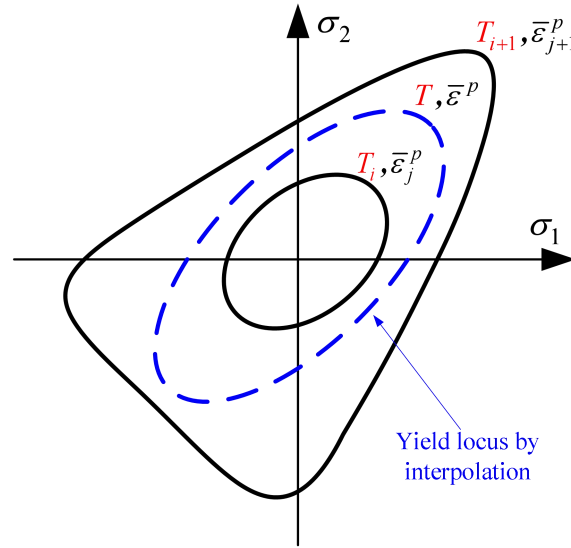
3.1 Temperature dependent discontinuous constitutive model

On the basis of the plastic theory, under certain deformation conditions, such as temperature and strain rate, the yield condition can be expressed as

$$f\left(\boldsymbol{\sigma},\bar{\varepsilon}^{p},T,\dot{\varepsilon}\right)=F\left(\boldsymbol{\sigma},\bar{\varepsilon}^{p},T,\dot{\varepsilon}\right)-\left[\Phi\left(\bar{\varepsilon}^{p},T,\dot{\varepsilon}\right)\right]^{a}=0 \tag{5}$$

where $F\left(\boldsymbol{\sigma},\bar{\varepsilon}^{p},T,\dot{\varepsilon}\right)$ is an expression with respect to the variable of $\boldsymbol{\sigma}$ and its value is related to equivalent plastic strain $\bar{\varepsilon}^{p}$, temperature T and strain rate $\dot{\varepsilon}$. $\Phi\left(\bar{\varepsilon}^{p},T,\dot{\varepsilon}\right)$ represents the size of yield loci and the value is determined by $\bar{\varepsilon}^{p}$, T and $\dot{\varepsilon}$.

For the continuous constitutive model, the yield loci at different strains are modelled by a specified model such as Hill'48 or CPB06 model. For the temperature dependent discontinuous constitutive framework, as shown in Fig. 12, the anisotropy/asymmetry-induced distorted yield loci at different strains and temperatures can be described by different constitutive models such as CPB06 model and Yoon's model. An interpolation approach is employed to smoothly representing the nonlinear evolution of distorted plasticity in the full stress space based on the established individual yield loci. The flow rules and the hardening laws are implicitly included in the temperature dependent discontinuous constitutive models.

Fig. 12. The temperature dependent discontinuous constitutive framework.

The proposed discontinuous constitutive framework has flexibility in selection of yield function. As shown in Fig. 12, only the limited individual yield loci at different strains and temperatures need to be established to describe the irregular evolution of the subsequent yielding. The sole constitutive model can be replaced by a mixed pattern of the different models, such as Hill'48+Yoon's and Hill'48+CPB06. For the deformation with a slight anisotropy at the small strain stage, the Hill'48 yield equations can be constructed to describe the evolution of

plasticity. The CPB06 model or the Yoon's model can be used to model the significant distortional hardening at the larger deformation stage.

Although several experimental procedures are available for testing materials under different strain paths, it is not always possible to probe them all. If the experimental data is not available for a given stress states, such as uniaxial tension along the normal direction for thin-walled materials, the VPSC-based simulation can be used to supplement the not complete experimental data for parameters calibration.

3.2 Numerical implementation of the discontinuous constitutive model

The above temperature dependent discontinuous constitutive framework is numerically implemented into the explicit FE platform by combining the implicit algorithm and interpolation approach. The detailed algorithms for implementation of constitutive models are stated in the previous study (Li et al., 2016; Yang et al., 2019). The interpolation approach for smoothly calculating the critical shear stress at arbitrary strain and temperature is described below.

- By using the yield stress data from the physical experiment and simulation, the anisotropic coefficients in the initial and subsequent yield surfaces corresponding to several certain equivalent plastic strains at certain temperatures ($T_1 < T_2 < \cdots < T_m , \bar{\varepsilon}_1^p < \bar{\varepsilon}_2^p < \cdots < \bar{\varepsilon}_n^p$) are obtained.

- The effective stress $\bar{\sigma}_i = \bar{\sigma}\left(\sigma_i, \bar{\varepsilon}_i^p, T\right)$ and the critical shear stress $\tau_i^Y = \tau^Y\left(\bar{\varepsilon}_i^p, T\right)$ and the expression $F\left(\sigma, \bar{\varepsilon}^p, T\right)$ at different strains and temperatures are calculated.

- For any given T ($T_i < T < T_{i+1}$) and $\bar{\varepsilon}^p$ ($\bar{\varepsilon}_j^p < \bar{\varepsilon}^p < \bar{\varepsilon}_{j+1}^p$), based on the interpolation approach, the distorted yield function can be determined by

$$f\left(\sigma, T, \bar{\varepsilon}^p\right) = F\left(\sigma, T, \bar{\varepsilon}^p\right) - \left[\Phi\left(T, \bar{\varepsilon}^p\right)\right]^a = 0 \tag{6}$$

where *a* is the exponent of the homogeneous yield functions, and

$$\begin{aligned} F\left(\sigma, T, \bar{\varepsilon}^p\right) = {} & \xi_{i,j} f_{i,j}\left(\sigma, T_i, \bar{\varepsilon}_j^p\right) + \xi_{i,j+1} f_{i,j+1}\left(\sigma, T_i, \bar{\varepsilon}_{j+1}^p\right) \\ & + \xi_{i+1,j} f_{i+1,j}\left(\sigma, T_{i+1}, \bar{\varepsilon}_j^p\right) + \xi_{i+1,j+1} f_{i+1,j+1}\left(\sigma, T_{i+1}, \bar{\varepsilon}_{j+1}^p\right) \end{aligned} \tag{7}$$

$$\Phi\left(T, \bar{\varepsilon}^p\right) = \left(\xi_{i,j}\left(\tau_{i,j}^Y\right)^a + \xi_{i,j+1}\left(\tau_{i,j+1}^Y\right)^a + \xi_{i+1,j}\left(\tau_{i+1,j}^Y\right)^a + \xi_{i+1,j+1}\left(\tau_{i+1,j+1}^Y\right)^a\right)^{1/a} \tag{8}$$

and the weight coefficients can be expressed as

$$\xi_{i,j} = \frac{\left(T_{i+1} - T\right)\left(\bar{\varepsilon}_{j+1}^p - \bar{\varepsilon}^p\right)}{\left(T_{i+1} - T_i\right)\left(\bar{\varepsilon}_{j+1}^p - \bar{\varepsilon}_j^p\right)} \tag{9}$$

$$\xi_{i,j+1} = \frac{\left(T_{i+1} - T\right)\left(\bar{\varepsilon}^p - \bar{\varepsilon}_j^p\right)}{\left(T_{i+1} - T_i\right)\left(\bar{\varepsilon}_{j+1}^p - \bar{\varepsilon}_j^p\right)} \tag{10}$$

$$\xi_{i+1,j} = \frac{\left(T - T_i\right)\left(\bar{\varepsilon}_{j+1}^p - \bar{\varepsilon}^p\right)}{\left(T_{i+1} - T_i\right)\left(\bar{\varepsilon}_{j+1}^p - \bar{\varepsilon}_j^p\right)} \tag{11}$$

$$\xi_{i+1,j+1} = \frac{\left(T - T_i\right)\left(\bar{\varepsilon}^p - \bar{\varepsilon}_j^p\right)}{\left(T_{i+1} - T_i\right)\left(\bar{\varepsilon}_{j+1}^p - \bar{\varepsilon}_j^p\right)} \tag{12}$$

In this way, it can ensure that the sum of the above four coefficients equals to one. When $T = T_i$ and $\bar{\varepsilon}^p = \bar{\varepsilon}_i^p$, $\xi_{i,i} = 1$, and when $T = T_{i+1}$ or $\bar{\varepsilon}^p = \bar{\varepsilon}_{i+1}^p$, $\xi_{i,i} = 0$, the observed distortions in the shapes of the yield loci can then be described.

3.3 Calibration method of the discontinuous constitutive model

To construct the discontinuous constitutive framework, the calibration of several discontinuous yield loci, as shown in Fig. 12, needs to be conducted. Taking the stress invariant-based criterion (SIM), such as the Yoon's yield model designated in Eq. (13), as an instance, the detailed calibration processes are presented.

$$f(\boldsymbol{\sigma}) = bI_1(\boldsymbol{\sigma}) + \left[\left(J_2(\Sigma^A)\right)^{3/2} - J_3(\Sigma^B)\right]^{1/3} - \tau^Y = 0 \tag{13}$$

where I_1 is the first stress invariant and b is a material constant, $J_2(\Sigma^A)$ is the second stress invariant of the transformed stress tensor of Σ^A, $J_3(\Sigma^B)$ is the third stress invariant of another transformed stress tensor of Σ^B, $\Sigma^A = L_A[\boldsymbol{\sigma}]$, $\Sigma^B = L_B[\boldsymbol{\sigma}]$, L_A and L_B are two distinct fourth-order linear transformation tensors denoted in Eqs. (6) and (7). For plane stress state, a_4, a_5, b_4 and b_5 are all equal zero. For cold rolled sheet metals, the pressure insensitivity is assumed for yielding and hardening. Thus, the material constant b is set to zero.

$$\boldsymbol{L}_A = \begin{bmatrix} (a_3 + a_2)/3 & -a_3/3 & -a_2/3 & 0 & 0 & 0 \\ -a_3/3 & (a_1 + a_3)/3 & -a_1/3 & 0 & 0 & 0 \\ -a_2/3 & -a_1/3 & (a_1 + a_2)/3 & 0 & 0 & 0 \\ 0 & 0 & 0 & a_4 & 0 & 0 \\ 0 & 0 & 0 & 0 & a_5 & 0 \\ 0 & 0 & 0 & 0 & 0 & a_6 \end{bmatrix} \tag{14}$$

$$L_B = \begin{bmatrix} (b_3+b_2)/3 & -b_3/3 & -b_2/3 & 0 & 0 & 0 \\ -b_3/3 & (b_1+b_3)/3 & -b_1/3 & 0 & 0 & 0 \\ -b_2/3 & -b_1/3 & (b_1+b_2)/3 & 0 & 0 & 0 \\ 0 & 0 & 0 & b_4 & 0 & 0 \\ 0 & 0 & 0 & 0 & b_5 & 0 \\ 0 & 0 & 0 & 0 & 0 & b_6 \end{bmatrix} \tag{15}$$

For Yoon's model, eight parameters (a_1, a_2, a_3, a_4, b_1, b_2, b_3, b_4) are related to the in-plane plastic deformation behavior. They are calibrated by four uniaxial tensile yield stresses in the rolling direction (RD), the direction at an angle of 45° to RD, the transverse direction (TD) and the equibiaxial tension yield stress respectively denoted as T_0, T_{xy45}, T_{90} and T_b, and four compressive yield stresses along the same orientations designated as C_0, C_{xy45}, C_{90} and C_b. With the material constants identified above, the proposed yield function is able to describe the anisotropic and asymmetrical plasticity of the materials under the plane stress condition.

In the x-y plane, the uniaxial yield stresses designated as $T_{xy}(\theta)$ and $C_{xy}(\theta)$ are measured from in-plane uniaxial tensile and compressive tests in a direction with an angle of θ to the RD. The stress components of $T(C)_{xy}(\theta)$ for tension and compression in the orthotropic coordinate are obtained and formulated as:

$$\sigma_{xx} = T(C)_{xy}(\theta)\cos^2\theta, \quad \sigma_{yy} = T(C)_{xy}(\theta)\sin^2\theta, \quad \sigma_{xy} = T(C)_{xy}(\theta)\sin\theta\cos\theta \tag{16}$$

By substituting Eq. (16) into Eq. (13), the uniaxial tensile and compressive yield stresses in the x-y plane are obtained.

In addition, the R-value can also be used to determine the model parameters. The R-value in θ-direction from the RD under tension is represented as R_θ and calculated by the following equation:

$$R_\theta = \frac{d\varepsilon_{\theta+90°}}{d\varepsilon_{zz}} = \left(\frac{\partial F}{\partial \sigma_{xx}}\sin^2\theta + \frac{\partial F}{\partial \sigma_{yy}}\cos^2\theta - \frac{\partial F}{\partial \sigma_{xy}}\sin\theta\cos\theta\right) \bigg/ \left(-\frac{\partial F}{\partial \sigma_{xx}} - \frac{\partial F}{\partial \sigma_{yy}}\right) \tag{17}$$

By comparing the predicted yield stress and R-value with the experimental ones, an error function is constructed as below:

$$Error = \sum_i (T_i^{exp}/T_i^{pre} - 1)^2 + \sum_j (R_j^{exp}/R_j^{pre} - 1)^2 \tag{18}$$

where the superscript 'pre' and 'exp' represent the predicted value and the experimental data, respectively.

This objective function is constructed based on the Weight-Sum approach where the weight factors for all experimental values are set to 1. By minimizing the error function using the genetic algorithm (MALAB), the anisotropy parameters can be determined.

4. Results and discussion

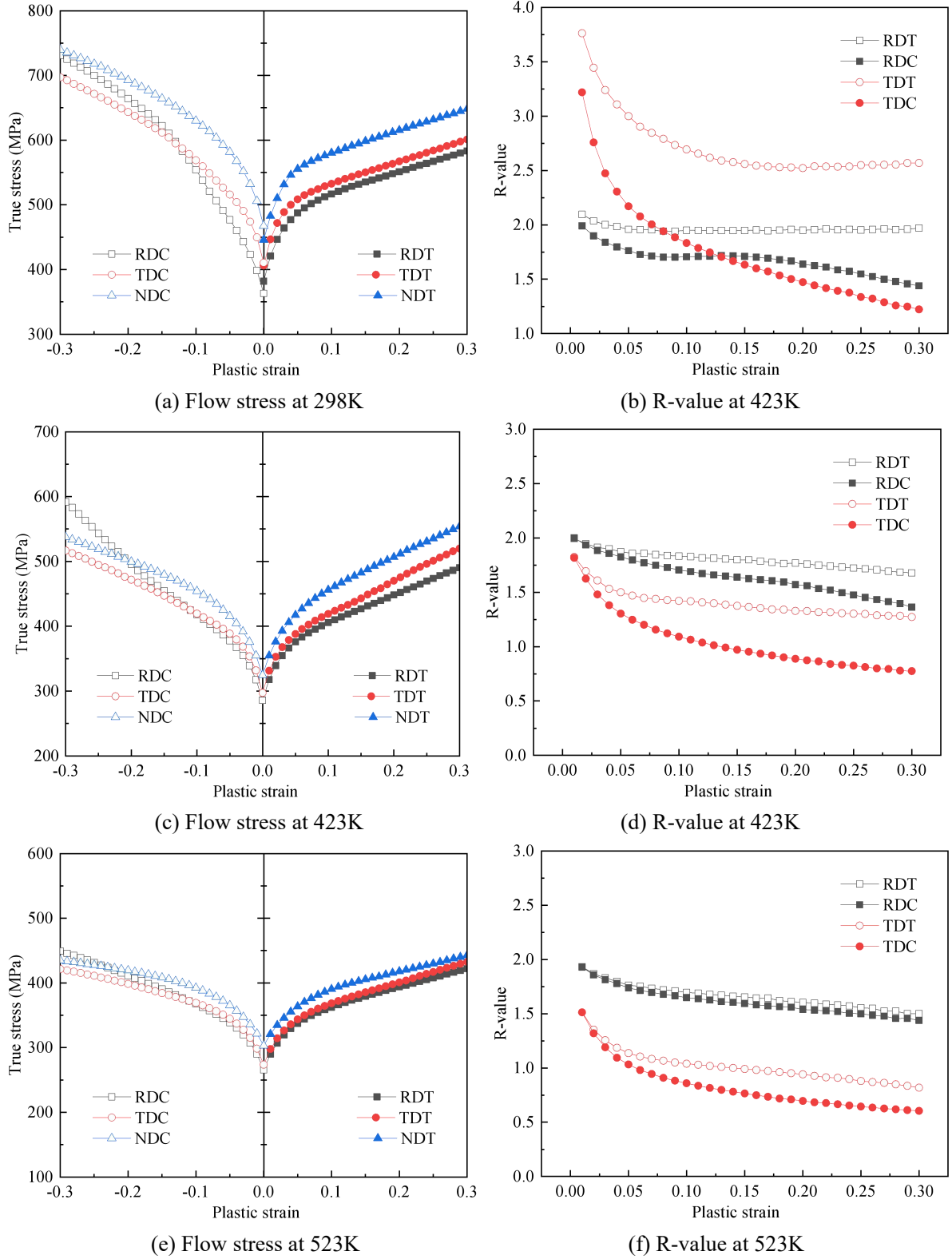### 4.1 Temperature dependent deformation behaviors and mechanisms

As mentioned in Section 2.1.2, the T-C asymmetry of flow stress is decreased with the increase of temperature, which indicates that the deformation modes change. In this section, by using the VPSC-based modeling with the calibrated material parameters, the plastic deformation of α-Ti tube under the six loading conditions at 298, 423 and 523K is studied. The effects of the temperature on anisotropy and asymmetry in terms of flow stress and R-value are first elaborated. The change of the relative activities of deformation modes with respect to strain and temperature, as well as its effects on texture evolution, is then examined. The effect of temperature on the correlation between plasticity behavior and deformation mechanism is also thoroughly discussed.

4.2.1 Temperature dependent anisotropic and asymmetrical plasticity

Fig. 13 shows the evolution of flow stress and R-value with strain for α-Ti tube at different temperatures. From Fig. 13(a), the flow stress of α-Ti tube at 298K shows a significant anisotropy in both tension and compression. Meanwhile, the T-C asymmetry is observed and gradually increased with plastic strain. Furthermore, the R-value also shows a remarkable anisotropy and asymmetry, as shown in Fig. 13 (b). The asymmetry of R-value along the TD is greater than that along the RD. The reason is that the R-value along the RD is decided by the deformation along the TD and ND, while the R-value along the TD is decided by the deformation along the RD and ND, and the T-C asymmetry of plastic deformation along the RD is greater than that along the TD. The R-value in tension along the RD is close to 2.0 and changes little, but it is steady decreased in compression. For the TD, the R-value in tension is first rapidly decreased and then stabilized with the increase of plastic strain, while it is gradually decreased in compression.

With the increase of temperature, there is a significant reduction of the anisotropy and asymmetry for the flow stress of α-Ti tube. From Fig. 13(e), the α-Ti tube shows a slight anisotropy and T-C asymmetry of the flow stress at 523K. For R-value, the obvious anisotropy also remains but the T-C asymmetry is decreased remarkably at elevated temperature. The asymmetry along the TD is still greater than that along the RD. All the R-values are gradually

decreased with the increase of plastic strain in tension and compression. At 523K, the R-value shows the initial T-C symmetry and its asymmetry is slightly increased with strain, as shown in Fig. 13(f).

(a) Flow stress at 298K

(b) R-value at 423K

(c) Flow stress at 423K

(d) R-value at 423K

(e) Flow stress at 523K

(f) R-value at 523K

Fig. 13. Flow stress and R-value of α-Ti tube at different working temperatures.

4.2.2 Temperature dependent deformation mechanisms

4.2.2.1 Deformation mode at different temperatures

In Fig. 14, it shows that the tension deformation along the RD is dominated by the Pr with a low CRSS over the entire range of plastic strain at room temperatures. The Ba and Py also make some contribution to the plastic deformation, but the Tt and Ct have no contribution. With the increase of temperature, the relative activity of Pr is reduced, the activity of Ba changes little, and the activity of Py is increased obviously. The reason is that the CRSS values for thermally activated slips decrease with the increasing temperature (Williams et al., 2002; Zeng et al., 2009b), and the reduction of the CRSS of Py is greater than that of Pr. Due to the fact that the initial texture with respect to the loading direction places many grains in a favorable orientation for Pr slipping, the deformation is always dominated by Pr at three working temperatures. At 298K, the fraction of Pr, Ba and Py change a little bit with strain due to the little change of the orientation of grains for the Pr dominated deformation. At elevated temperature, with the increase of strain, the fraction of Pr is decreased, the fraction of Ba is decreased slightly, and the fraction of Py is increased. This attributes to that the increased activity of Py makes the reoriented grains more suitable for the Py slipping rather than the Pr and Ba slipping.

For the compression along the RD, the fraction of Pr at 298K is gradually decreased with the increase of strain due to the change of grain orientation during the deformation, while the fraction of Ba and Py is increased obviously with strain. The relative activity of Tt is first increased sharply and then slowly decreased with the increase of strain. The reason is that the twinning makes the reoriented grains suitable for Ba and Py slipping. At elevated temperatures, owing to the fact that the thermally activated slipping suppresses the temperature insensitive twinning, the relative activity of Tt is decreased. Because of the unsuitable loading direction and the high CRSS value, the activity of Ct is still negligible at the three working temperatures. By comparing Figs. 13 and 14, it is the difference in the activity of Tt between tension and compression that mainly leads to the significant T-C asymmetry of flow stress and R-value (Hama et al., 2017; Yi et al., 2016). With the increase of working temperature, Tt becomes less active and the slip activities are very similar in tension and compression, which is responsible for the reduction of T-C asymmetry.

(a) RDT at 298K   (b) RDC at 298K

(c) RDT at 423K   (d) RDC at 423K

(e) RDT at 523K   (f) RDC at 523K
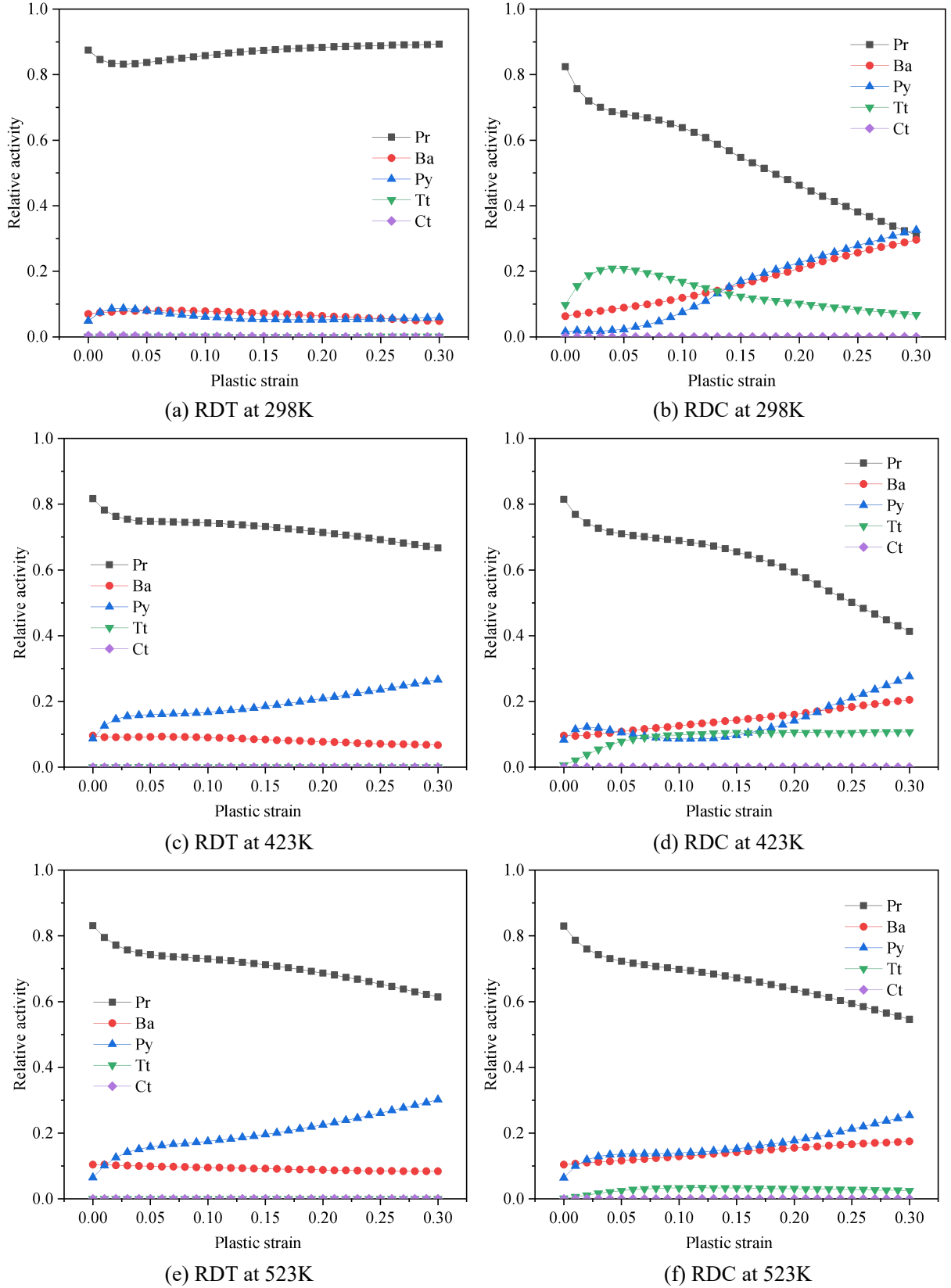
Fig. 14. Deformation modes for the RDT and RDC at different temperatures.

When subjected to the deformation along TD, as shown in Fig. 15, except for Pr, Ba is also the main deformation mode. Especially in compression, the relative activities of Ba are greater

than that of Pr when the strain is large than 0.1. With the increase of temperature, the fraction of Pr is decreased and the fraction of Ba is increased. This suggests that the reduction of the CRSS of Ba is greater than that of Pr, and the Ba is much easier to be activated along TD than   RD.

The fraction of Py is negligible during the tension at 298K, while it is increased with strain in compression. With the increase of temperature, the relative activity of Py is increased but always less than that of Ba, which indicates that, for the deformation along TD, the orientations of grains are more suitable for the activation of Ba rather than Py. At the three working temperatures, the fraction of Py in tension is all lower than that in compression, which reveals that compression is more beneficial to the activation of Py than tension. For compression, the relative activity of Pr is decreased with the increase of strain, while that of Ba and Py is increased gradually with strain. The reason is that the compression could rotate the grains to the preferable orientation for Py rather than Pr and Ba.

The relative activity of Tt in compression is greater than that in tension due to the direction dependence of twin, but the fractions are only few. With the increase of temperature, Tt become less active, and Ct is still negligible. At 523K, the deformation is mainly coordinated by slip systems. This attributes to the fact that the activation of Py inhibits twinning activity, which also results in the decrease of the T-C asymmetry of flow stress and R-value.
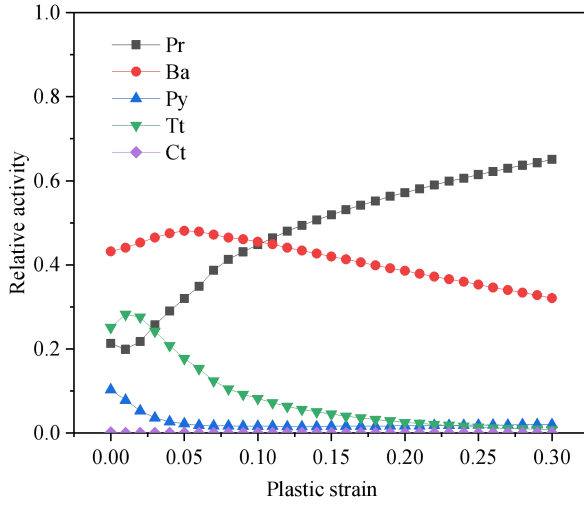

(a) TDT at 298K   (b) TDC at 298K

(c) TDT at 423K

(d) TDC at 423K


(c) TDT at 523K
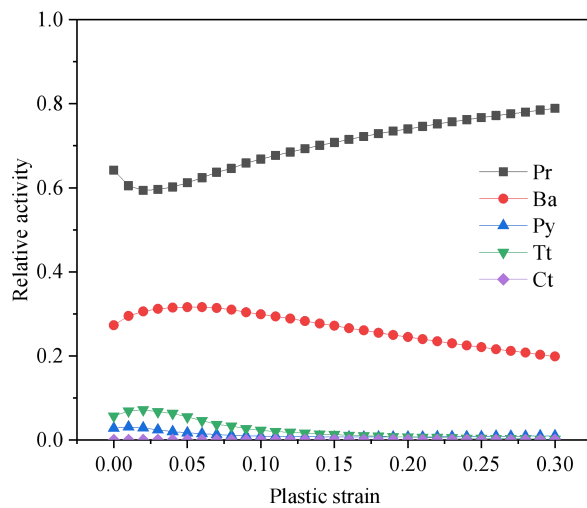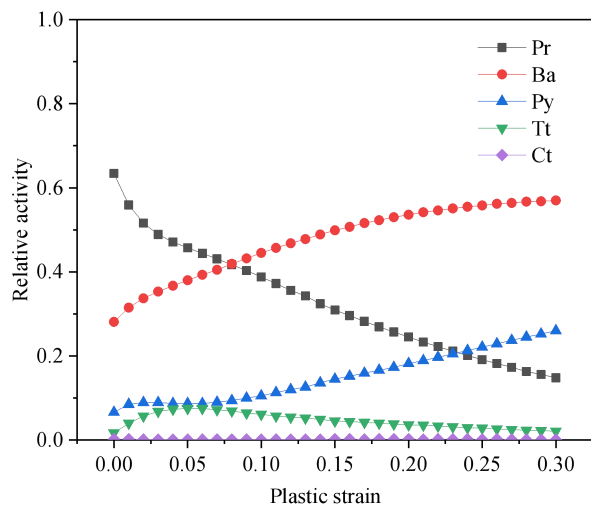
(d) TDC at 523K
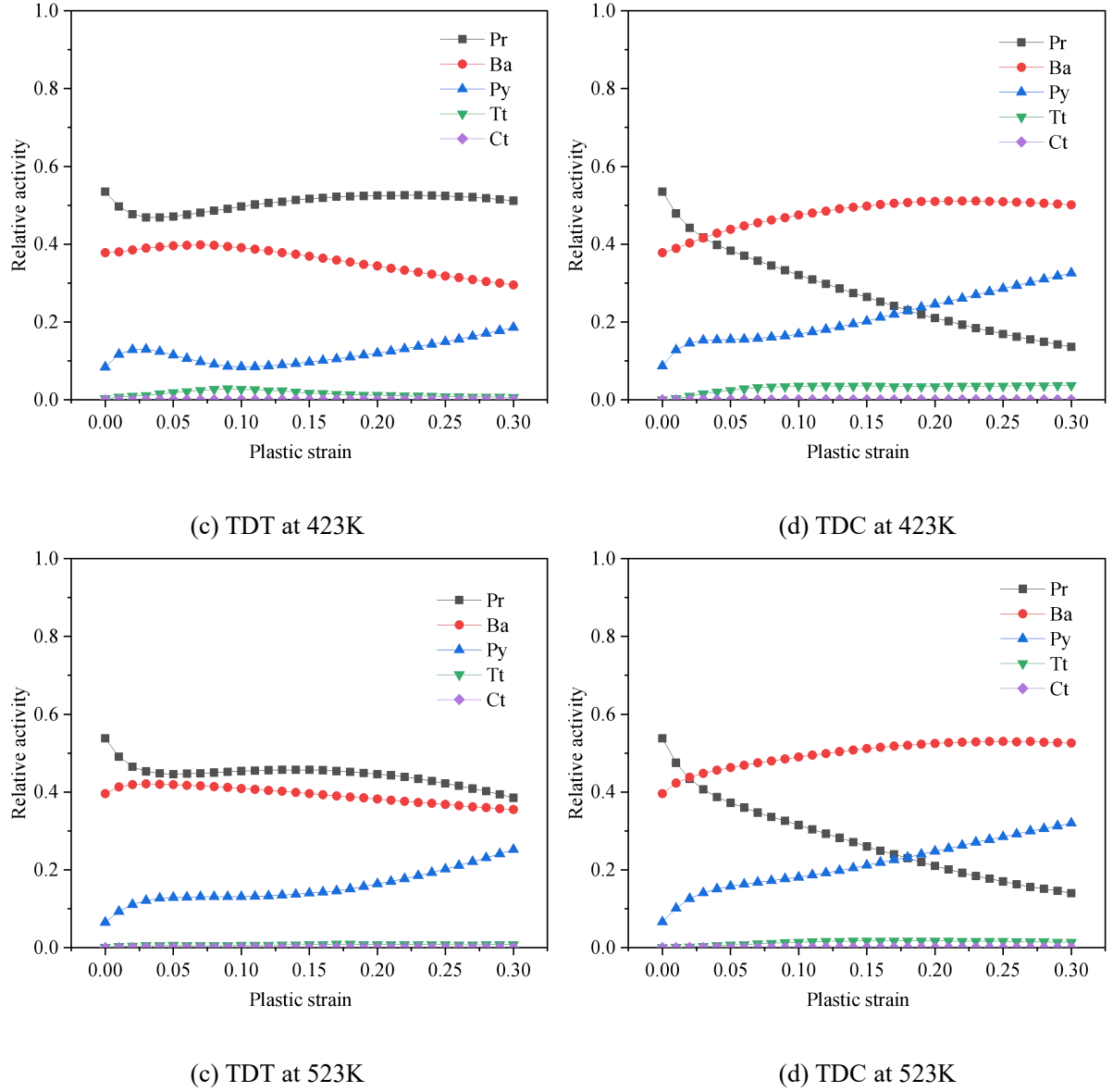
Fig. 15. Deformation modes for the TDT and TDC at different temperatures.

Unlike RD and TD loadings, when subjected to deformation along ND, the loading direction is almost parallel to the c-axis of a large fraction of grains. For the tension at 298K, as shown in Fig. 16(a), Tt is activated largely at the beginning due to the fact that the initial texture with respect to the loading direction places many grains in a favorable orientation for twinning. Subsequently, the twinning activity is decreased with the increase of strain, and the fraction of Pr is increased with strain due to the reoriented grains with suitable orientations for slipping. With the reorientation of grains, the fraction of Ba is first increased slightly and then gradually decreased. With the increase of working temperature, the fraction of Ba changes little and Pr and Tt become less active, but Py becomes more active in coordinating the deformation along the c-axes of grains. This reveals that the deformation along the c-axis of grains is mainly

coordinated by Tt at room temperature, and by Py at elevated temperature (Bishoyi et al., 2017; Zeng et al., 2009b). For compression, due to the unsuitable loading direction for twinning, Py is activated to coordinate the deformation along the c-axes of grains. At the three working temperatures, the deformations are all dominated by slip, but the twinning activity is negligible.
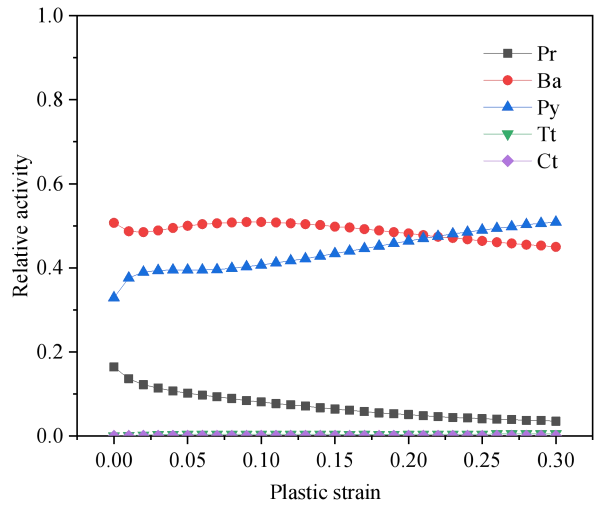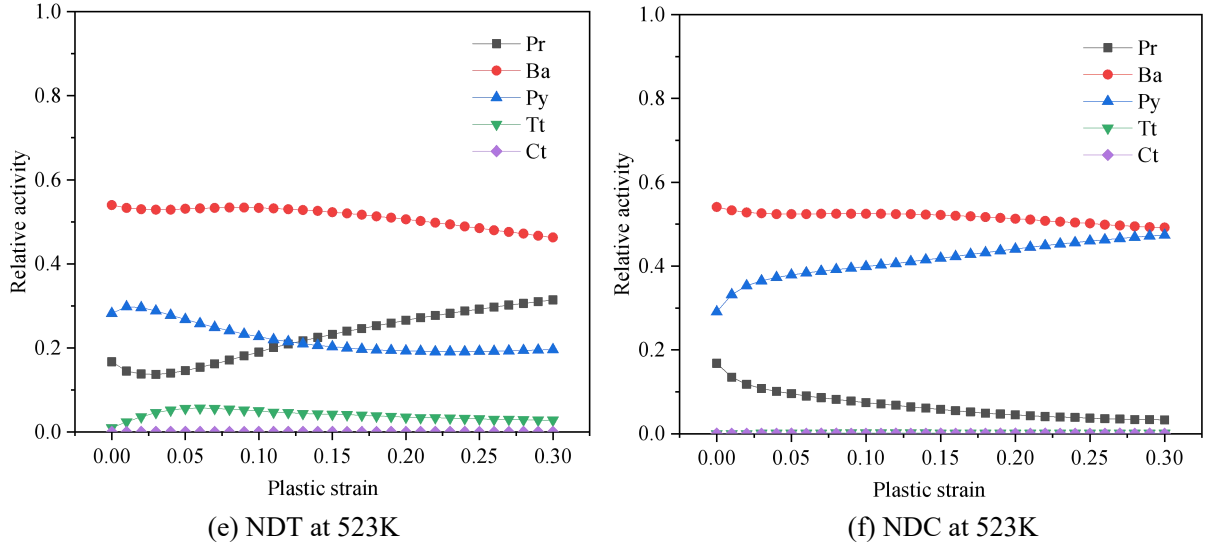

(a) NDT at 298K
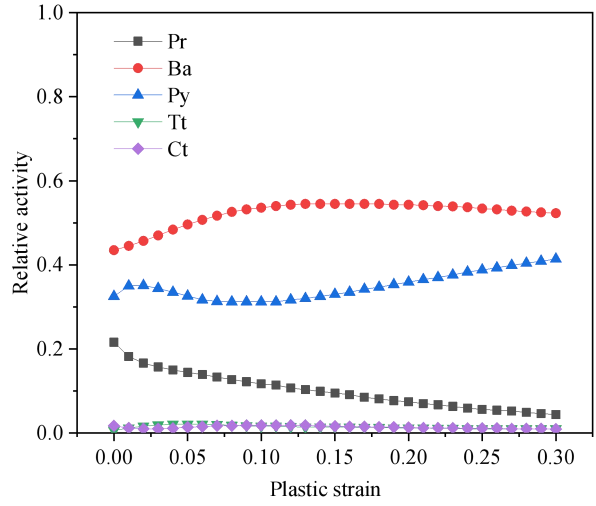
(b) NDC at 298K
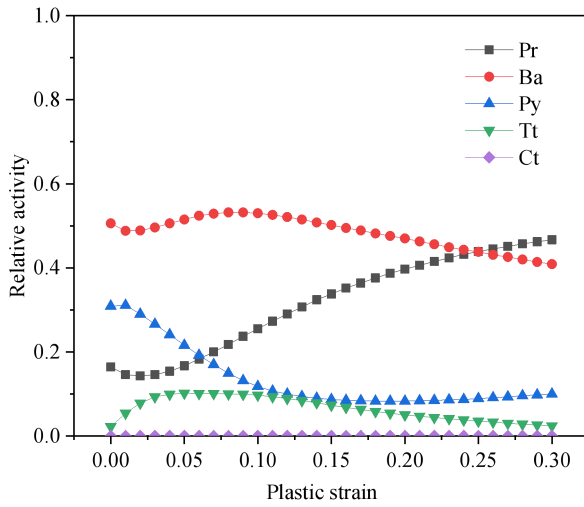
(c) NDT at 423K

(d) NDC at 423K

(e) NDT at 523K   (f) NDC at 523K

Fig. 16. Deformation modes for the NDT and NDC at different temperatures.

4.2.2.2 Texture evolution with temperature

The change of the relative activity of individual deformation modes under different thermal-mechanical loading conditions surely induces diverse texture, which is one of the root causes of the distorted evolution of plasticity with temperature. Table 8 shows that the texture evolution of α-Ti tube with temperature presents the significant anisotropy and asymmetry for six typical loading conditions. For the tension along RD, the pole figures change little with temperature and maintain the bimodal distribution due to the fact that the orientation of grains changes little for the Pr dominated deformation. However, for the compression along RD, the activation of Tt causes a nearly 90° rotation of crystal structure from ND to RD. With the increase of temperature, the reduction of the relative activity of Tt weakens the change of texture. At 523K, only a small quantity of rotations of grains are observed.

When subjected to the tension along TD, the activation of Tt also makes the c-axes of a few grains rotate to RD at 298K. For the tension along ND, the c-axes of grains rotate to RD and TD. For the compression along TD, the c-axes of grains are toward to TD. These suggest that the activation of Tt rotates the c-axes to the loading direction in compression, while towards the direction perpendicular to the loading direction in tension. The increase of temperature reduces the relative activity of Tt, and further weakens the tendency of grain rotation caused by twinning. For the compression along ND, the textures change a bit with temperature owing to the fact that the deformation is dominated by slipping.

In brief, the distorted evolution of anisotropic and asymmetrical plasticity with temperature and strain comes from the change of the relative activities of Pr, Ba, Py, Tt and Ct. The slipping gradually rotates the c-axes of grains, butTt causes a sudden rotation with nearly 90 degrees in

33

the grain orientation. It is the increase of the relative activity of slip with temperature that suppresses the activity of Tt and weakens the change of texture. The reduction of the twin activity decreases the T-C asymmetry in terms of flow stress and R-value. The activation of Tt at 298K makes the texture change drastically and α-Ti tube presents the obvious anisotropy and asymmetry of deformed textures. At elevated temperature, for the six loading directions, the deformations are all dominated by Pr, Ba and Pr. The difference in the relative activities of slip systems along the six loading directions makes the grains rotate diversely, but the textures all present the bimodal distribution due to the reduced rotation of grains. The coupling of the similar texture and the same deformation mechanism accounts for the significantly reduced anisotropy and asymmetry of flow stress at 523K.

Table 8 Predicted (0001) pole figures after 20% tension/compression along six directions for α-Ti tube at different temperatures.
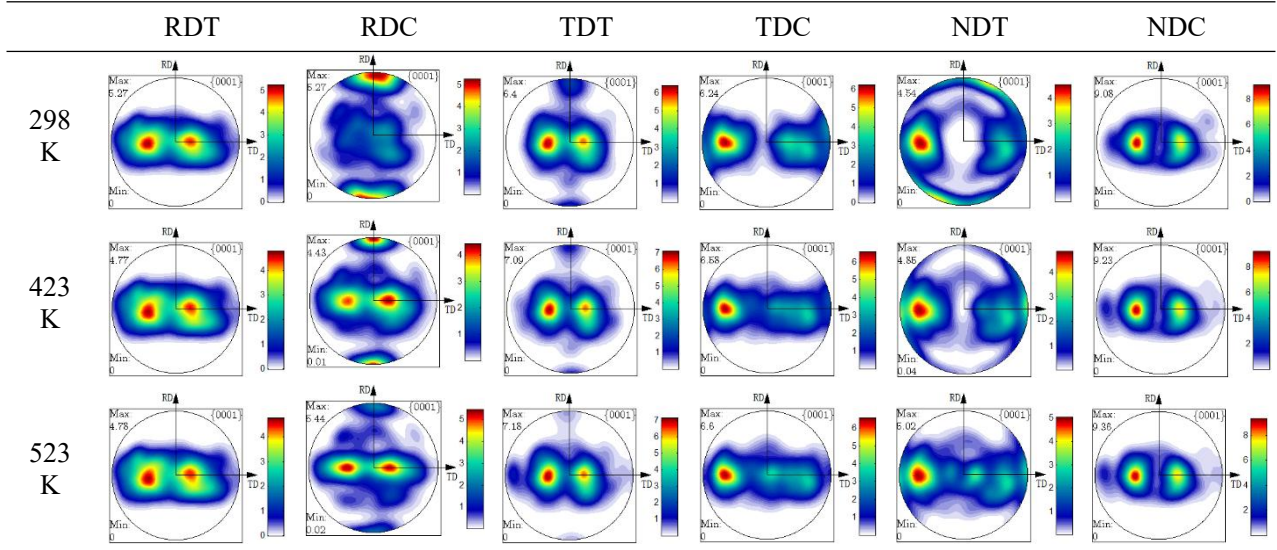
4.2 Effect of deformation mechanism on the anisotropy and asymmetry of plasticity

From the above research, the evolution of anisotropy and asymmetry of plasticity behaviors with temperature is mainly generated due to the change of deformation mechanism. Therefore, it is necessary and critical to determine the correlation of deformation mechanism and the anisotropy and asymmetry of materials. Due to the fact that Pr, Ba, Tt or Ct without five independent slip/twin systems cannot satisfy the von Mises criterion (Yoo, 1981), the Py with twelve slip systems is combined with each of them. Accordingly, the seven combinations, comprising of Py, Pr and Py, Ba and Py, Pr, Ba and Py, Tt and Py, Ct and Py, Tt and Ct, are taken into account. Based on the model parameters of α-Ti tube at 298K, the VPSC-based simulations are conducted to explore the effect of deformation mechanism on the anisotropy and

asymmetry of plasticity, and further the coordination and competition of different deformation modes.


4.2.1 Role of the deformation mechanisms on plasticity

4.1.1.1 Flow stress in different deformation modes

Fig. 17 shows the true stress-strain curves of α-Ti tube under different deformation mechanisms and loading conditions at 298K. It can be seen that the α-Ti tube has a significant anisotropy in both tension and compression with the deformation mechanisms studied. The initial yield stress shows the T-C symmetry for slip systems but the T-C asymmetry for twin systems. With the increase of strain, when Py, Tt or Ct is activated, the T-C asymmetry of flow stress occurs and significantly increases. The activation of Pr and Ba is conducive to reducing the T-C asymmetry. Considering only slip systems, true stress is increased with strain in tension or compression deformation along RD, TD and ND. When only twin systems are activated, the α-Ti tube shows a remarkable and alternately hardening and softening behaviors.

From Fig. 17(a), when only the pyramidal slip operates, the α-Ti tube at a large strain presents a slight T-C asymmetry in the flow stress along RD and TD, but an obvious one along ND. The flow stress in tension along RD, TD and ND is the highest, intermediate and lowest value, respectively. The reason is that Py mainly coordinates the deformation along the c-axes, and the c-axis of a large fraction of grains is almost parallel to ND. Compared with Py, the smaller CRSS for Pr significantly reduces the flow stress, especially along RD and TD, as shown in Fig. 17(b). Whether in tension or compression state, the flow stress along ND, TD and RD is the highest, intermediate and lowest, respectively. This attributes to that the initial texture with respect to RD places many grains in a favorable orientation for Pr slipping. Compared with the activation of Py only, from Fig. 17(c), the activation of Ba with a low CRSS can significantly reduce the flow stress along the TD and ND, which suggests a high activity of Ba along these directions. From Fig. 17(d), the activation of Tt leads to the significant T-C asymmetry along RD and TD, but it can be negligible along ND. The flow stress in compression is all less than the one in tension for RD and TD. Compared with Fig. 17(a), Fig. 17(e) shows that the activation of Ct has a little effect on flow stress.

By comparing Fig. 17(f) with Fig. 17(a), when Pr, Ba and Pr are all activated, the flow stress is decreased obviously and shows the slight T-C asymmetry at the large strain. The flow stress in compression is all greater than the one in tension for RD, TD and ND. The stress along ND, TD and RD is the highest, intermediate and lowest, respectively. When only the Tt and Ct are activated, as shown in Fig. 17(g), the flow stress of α-Ti tube shows the significant

anisotropy and asymmetry, and an alternation of hardening and softening is observed. This suggests that the twinning has much more contributions to the distorted evolution of plasticity. Due to the larger CRSS of twinning compared with slipping, the yield stress in tension and compression is all greater than that when the slip systems are activated.
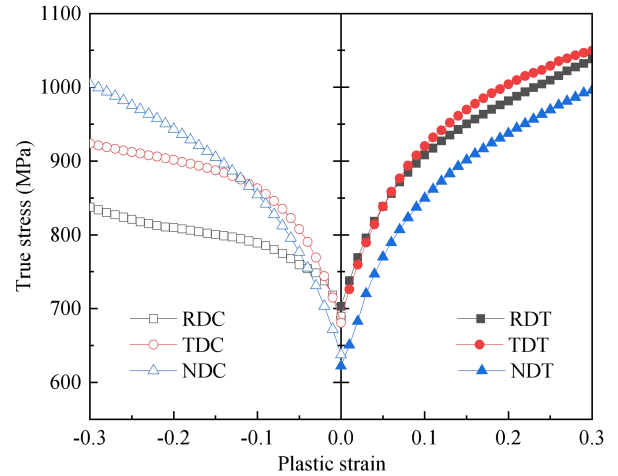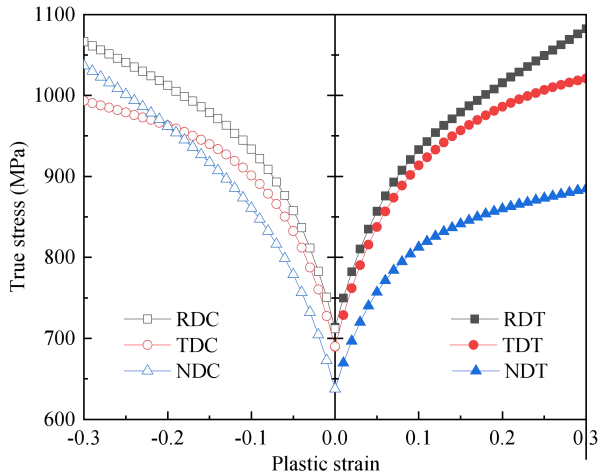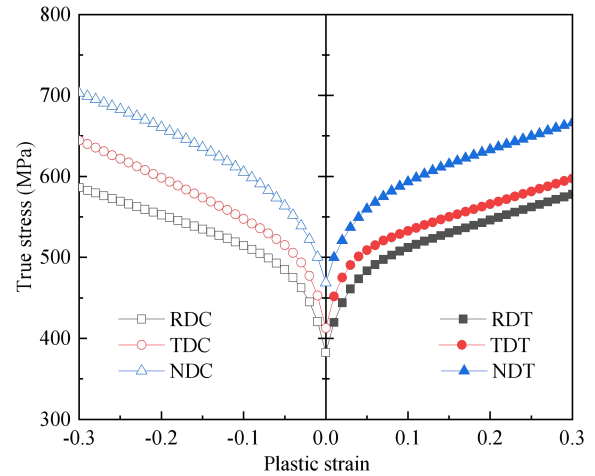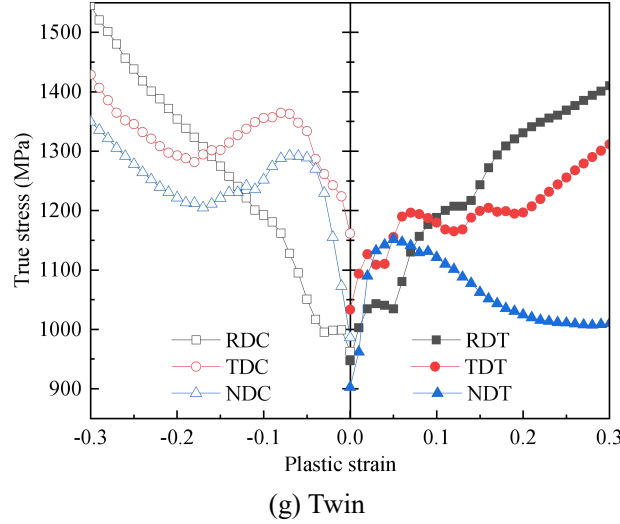

(a) Py

(b) Py+Pr

(c) Py+Ba

(d) Py+Tw

(e) Py+Cw

(f) Slip

(g) Twin
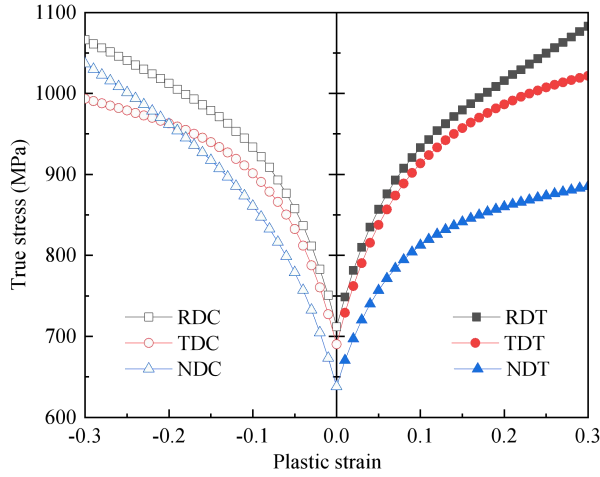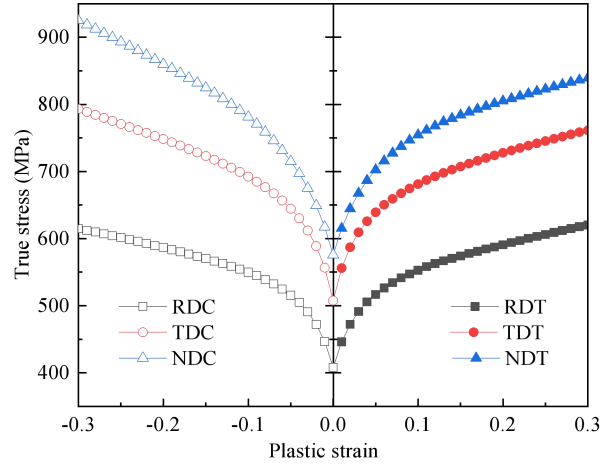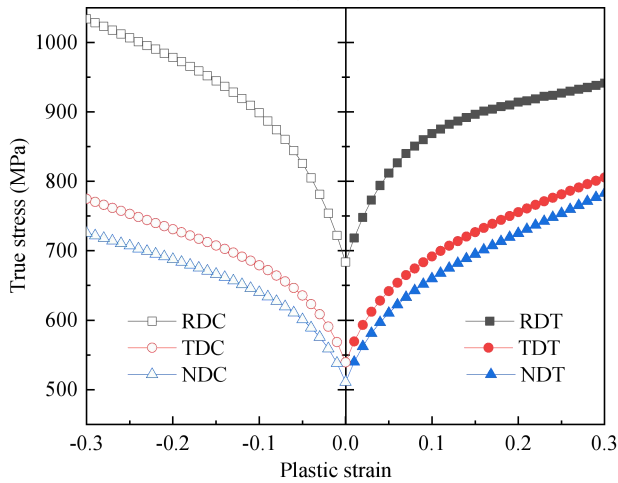
Fig. 17. True stress-plastic strain curves of α-Ti tube with different deformation mechanisms.

4.1.1.2 R-value for different deformation modes

Fig. 18 shows the evolution of R-value under RDT, RDC, TDT and TDC for α-Ti tube with different deformation mechanisms. It is found that there is the pronounced anisotropy and asymmetry of plastic flow. When Pr is activated, as shown in Figs. 18(b) and 18(f), the R-values along RDT, RDC, TDT and TDC, are all greater than one. When other deformation modes are activated but   Pr is excluded, the R-values are all less than one. The reason is that Pr cannot coordinate the deformation along the c-axes of grains, and the strain in ND is less than that in RD and TD in the Pr dominated deformation. Due to the capacity of coordinating the deformation along the c-axes, the Py would reduce the R-value of the materials that the c-axes of grains is towards to ND. This is true for Tt and Ct. Due to the fact that the activation of slip systems is identical for tension and compression, the initial R-value shows T-C symmetry, as shown in Fig. 18 (a), (b), (c) and (f). From Fig. 18 (d), (e) and (g), owing to the dependence of the activation of the twin systems in the loading direction, the initial R-value shows the obvious T-C asymmetry.

From Fig. 18(a), when Py is activated, the R-value in tension along RD and TD is increased with the plastic strain, but decreased in compression. No matter it is tension or compression, the R-value along RD is greater than the one along TD. This suggests that Py makes more contribution to the deformation along TD compared with RD. For the activation of Pr and Py, as shown in Fig. 18(b), the R-value along RD is first decreased and then remains nearly constant during tension deformation, but these along TD is drastically decreased with the increase of plastic strain. The R-value in compression along RD or TD is first sharply decreased then gradually increased with the increase of plastic strain. Fig. 18(c) reveals that the plastic flow

shows the T-C symmetry and the R-value remains approximately constant when Ba and Py are activated.

Fig. 18(d) shows when Tt and Py are activated, an obvious T-C asymmetry of R-value   along RD and TD exists. Generally,   the R-value is gradually increased and shows an obvious anisotropic and asymmetrical evolution. By comparing Figs. 18(e) with 18(a), the plastic flow changes little, due to the rarely activation of Ct.

When Pr, Ba and Py are all activated, as shown in Fig. 18(f), the R-value along RD shows the T-C symmetry and changes a bit with strain. While for TD, the significant asymmetry is observed and the R-value is first decreased, followed by an increase during tension, but it is steadily decreased during compression. For the activation of only twin systems, as shown in Fig. 18 (g), the R-value is rapidly increased first and then gradually decreased. The T-C asymmetry along TD is more pronounced than that along RD.
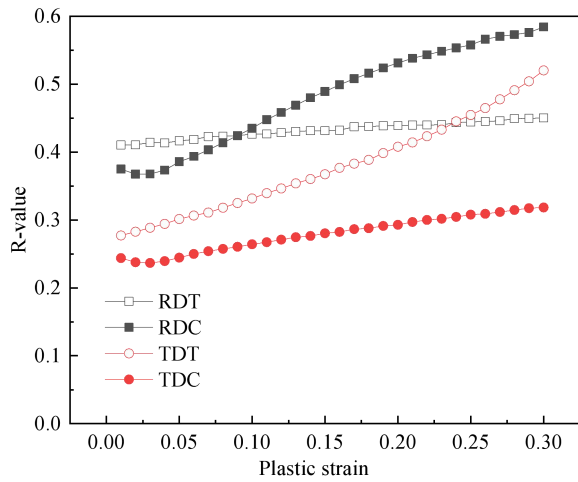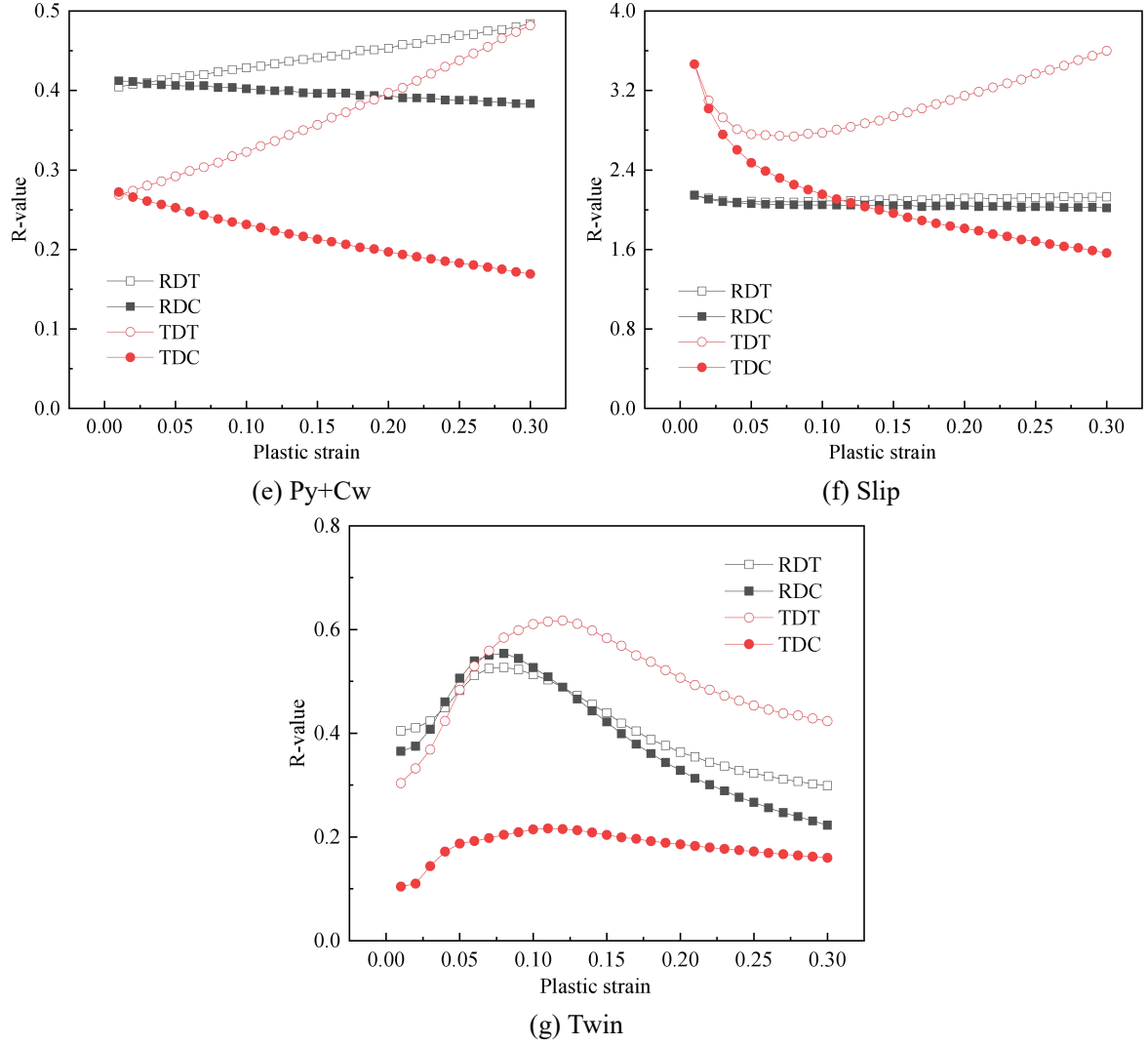

(a) Py

(b) Py+Pr

(c) Py+Ba

(d) Py+Tw

(e) Py+Cw

(f) Slip

(g) Twin
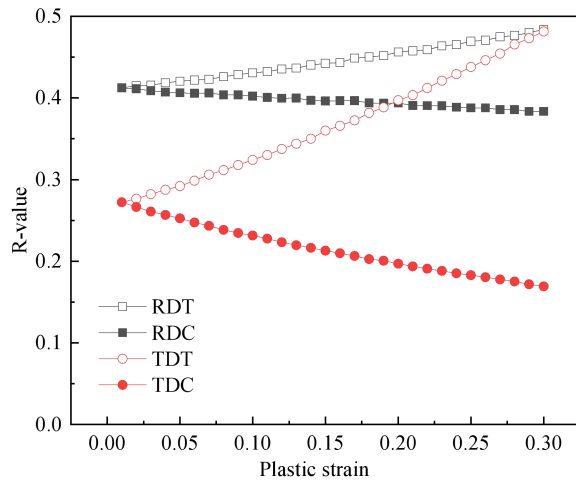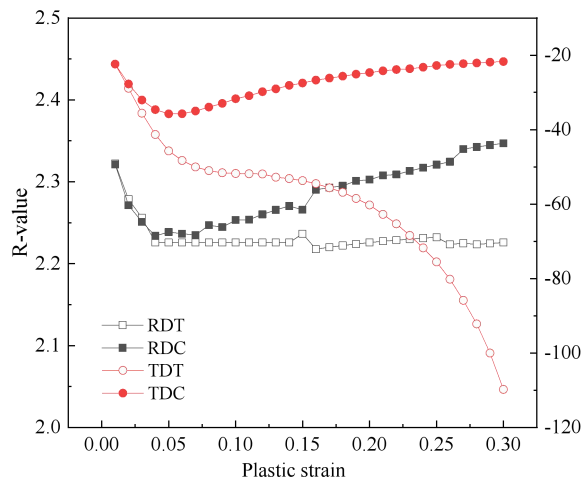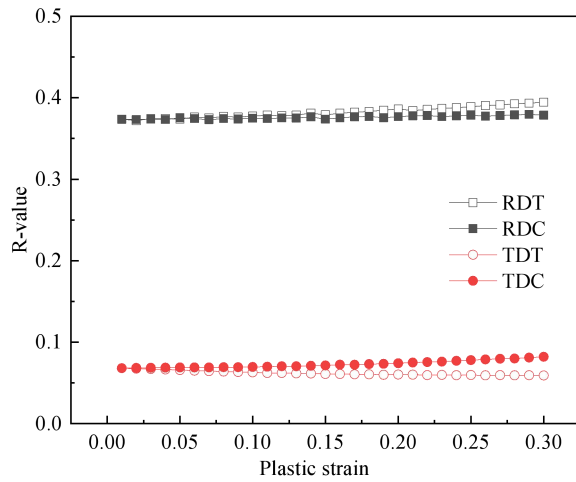
Fig. 18. The Plastic flow of α-Ti tube with different deformation mechanisms.

4.2.2 Mechanisms for coordinating the distorted plasticity

To clarify the mechanism of plastic anisotropy and asymmetry, the relative activities of individual deformation modes in the six combinations are calculated and analyzed. When only Py is activated in tension or compression, as shown in Table 9, the pole figures present the remarkable T-C asymmetry, no matter it is RD, TD or ND. The reason is the rotation of the normal direction of slip plane towards the loading direction in compression, while it rotates towards the direction perpendicular to the loading direction in tension (Mayama et al., 2009; Wang et al., 2018). In addition, Py makes the c-axes of grains rotate to ND under the RDC and TDC, which would contribute to the decrease in the thickness strain and further increase the R-value. And it is opposite for RDT and TDT. This accounts for the change of R-value with strain shown in Fig. 18(a). Due to the rotation of grains, the initial T-C symmetry of flow stress and R-value vanishes and the T-C asymmetry occurs with the increase of strain, as shown in

Figs. 17(a) and 18(a). Compared with the initial state shown in Fig. 2, the pole figures change slightly and remain the bimodal distribution under TDT, RDC and NDC. Under the RDT, four peaks appear, which reveals that the c-axes of grains have a degree of angular deflection along ND. Under NDT and TDC, nearly all the c-axes are toward to ND, and the pole figures show the unimodal pattern with the maximum density along ND. It is the different rotation and reorientation of grains during deformation that lead to the anisotropy and asymmetry in flow stress and R-value.

Table 9 The predicted (0001) pole figures after 20% tension/compression along six directions of α-Ti tube when Py is activated.
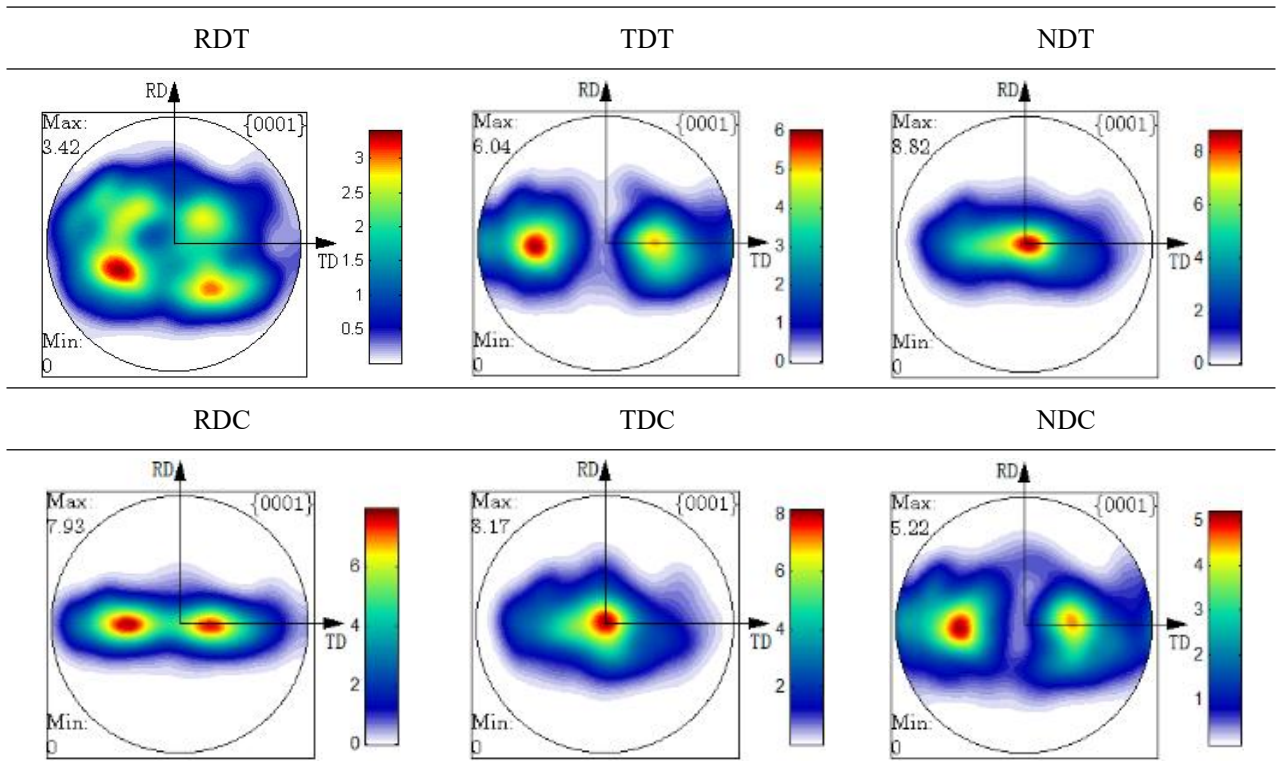

For the activation of Pr and Py, as shown in Fig. 19(a), the tension and compression deformation along RD are dominated by Pr with a low CRSS over the entire range of plastic strain. Meanwhile, there is the T-C symmetry in the relative activities of individual deformation modes, which accounts for the symmetry in flow stress along RD, as shown in Fig. 17(b). Due to the plastic flow determined by the deformation of two directions, there is an asymmetrical evolution of R-value with plastic strain, as shown in Fig. 18(b). For TD, from Fig. 19(b), Pr also dominates but the fraction of Py increases, resulting in the rise of flow stress. The deformation along c-axis of the HCP is mainly accommodated by **the** Py with a higher CRSS. Hence, when subjected to the loading along ND, as shown in Fig. 19(c), the fraction of Py is more than that of

Pr, the corresponding flow stress is highest. Due to the fact that the deformation along RD is dominated by Pr without the rotation to the c-axes of grains, from Fig. 19(d), the pole figures present the T-C symmetry. For TD, owing to the increase of the activity of Py compared with RD, the T-C asymmetry in the relative activities of individual deformation modes rises slightly, which makes the texture a slight change. For the deformation along ND, more obvious T-C asymmetry in the relative activities leads to a more remarkable asymmetry in the pole figures.
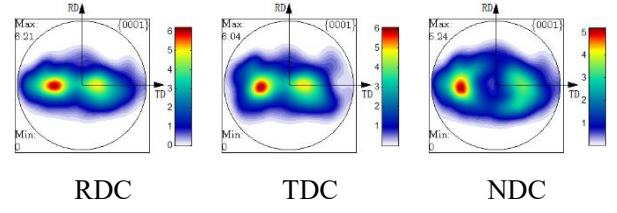

(a) RD

(b) TD

RDT　　　TDT　　　NDT

RDC   TDC   NDC
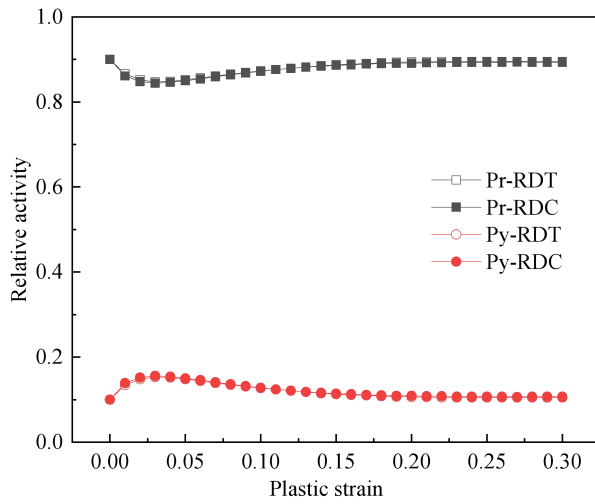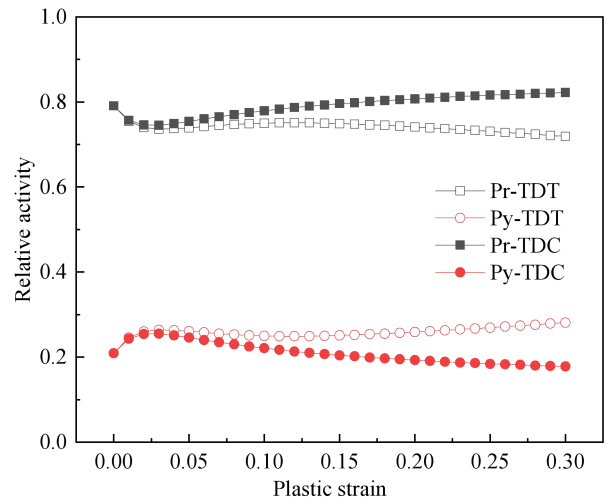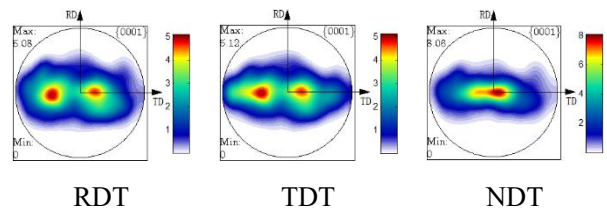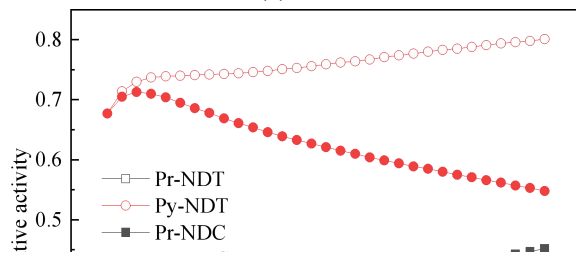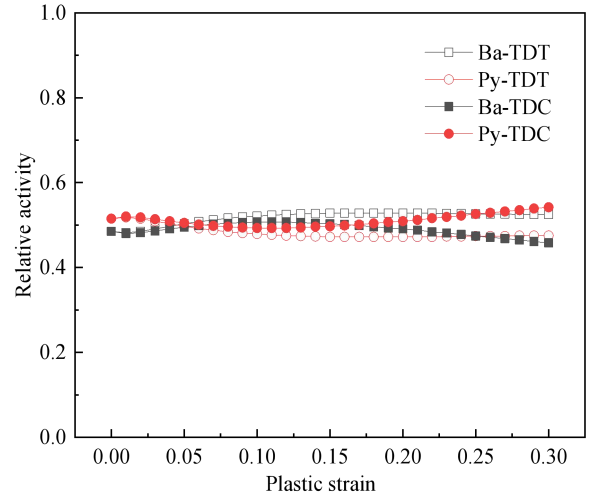
(c) ND   (d) Pole figures

Fig. 19. The role of prismatic and pyramidal slip during plastic deformation.

When Ba and Py are activated, as shown in Fig. 20, the relative activities of individual deformation modes present the obvious T-C asymmetry along RD, but slight one along the TD and ND. This accounts for the larger T-C asymmetry of flow stress along RD compared with TD and ND, as shown in Fig. 17(c). The fraction of Ba along ND, TD and RD is the highest, intermediate and lowest, respectively, which accounts for the relative magnitude of the flow stress. By comparing the pole figures shown in Table 9, the deformation along RD is dominated by Py and the effects of Ba on texture are covered. For the deformation along TD and ND, the fraction of Ba is similar to that of Py, and the textures show the bimodal distribution under TDT and NDC, and the three peaks distribution under TDC and NDT.
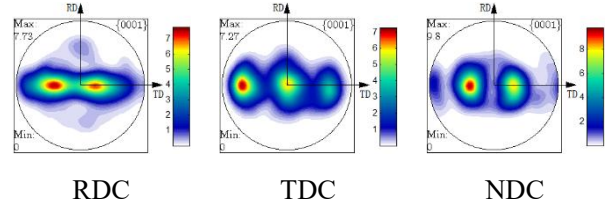
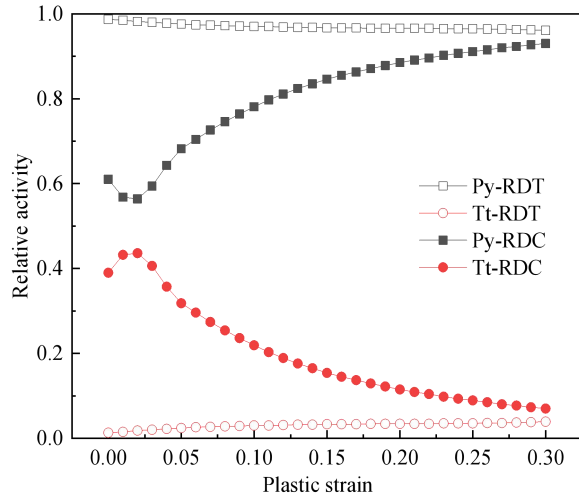

(a) RD   (b) TD

RDT   TDT   NDT

RDC   TDC   NDC
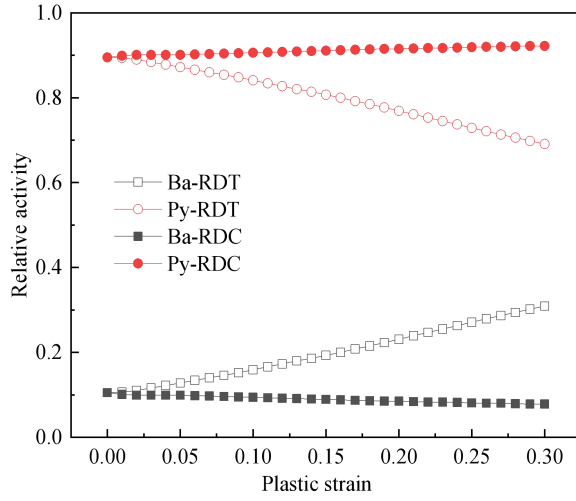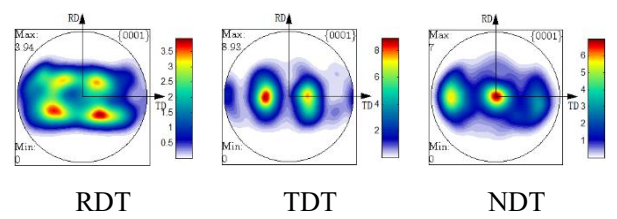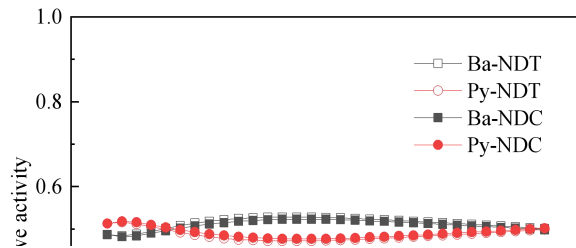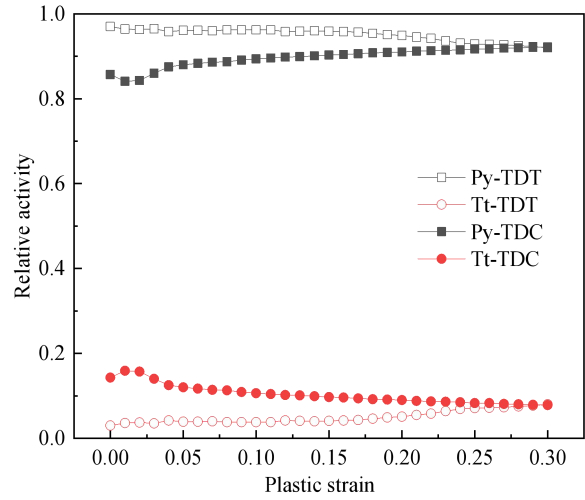
(c) ND   (d) Pole figures

**Fig. 20.** The role of basal and pyramidal slip during plastic deformation.

For the activation of Tt and Py, as shown in Fig. 21, due to the remarkable difference in the relative activities of Tt between tension and compression, the flow stress shown in Fig. 17(d) presents the significant T-C asymmetry. It should be pointed that there is a relatively large fraction of Tt at the early deformation stage of compression. At the later deformation stage, the role of Tt gradually weakens followed by an increase of the relative activities of Py. The reason is that Tt makes the c-axes of grains rotate to the loading direction in compression and perpendicularly to the loading direction in tension, which promotes the activity of Py. Accordingly, as shown in Fig. 21(d), the c-axes of almost all the grains rotate to RD under RDC, the c-axes of some grains rotate perpendicularly to ND under NDT, and towards TD under TDC. Under RDT, TDT and NDC, due to the less activity of Tt, the pole figures are close to these of the Py dominated deformation.

(a) RD

(b) TD

RDT   TDT   NDT

RDC   TDC   NDC
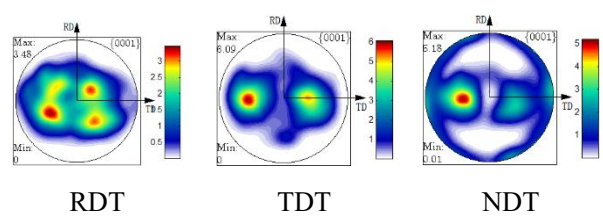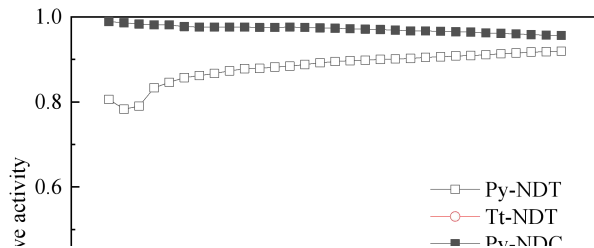
(c) ND   (d) Pole figures

Fig. 21. The role of pyramidal slip and tension twin during plastic deformation.

For the combination of Ct and Py, from Fig. 22, Ct is slightly activated only in the early deformation stage but the role of Py is overwhelming during the whole deformation stage, which reveals that Py has more advantages than Ct for accommodating the deformation along c-axis. Accordingly, the flow stress, plastic flow and pole figure under the activation of Py and Ct are practically identical to those under the activation of Py.

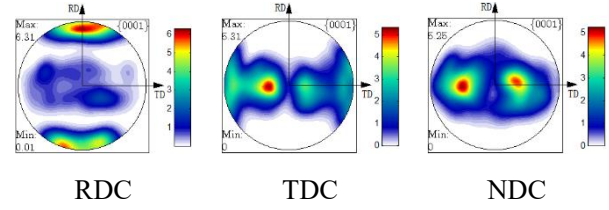(a) RD   (b) TD

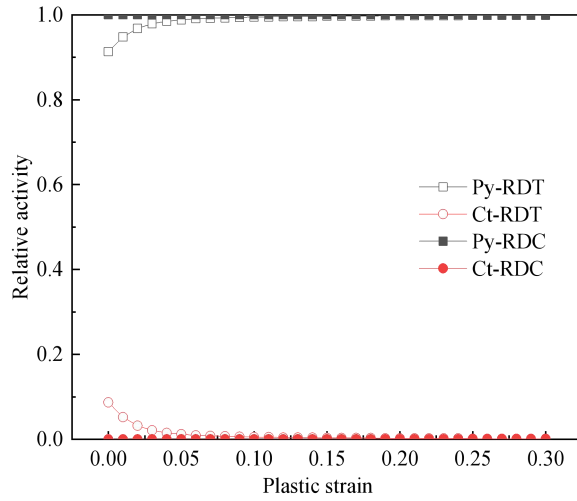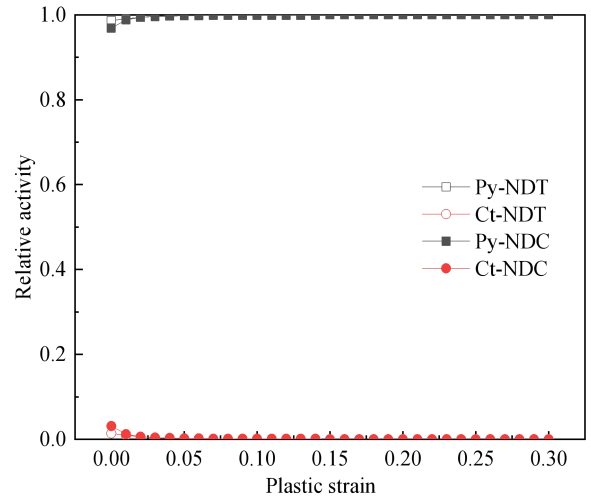RDT   TDT   NDT

RDC   TDC   NDC
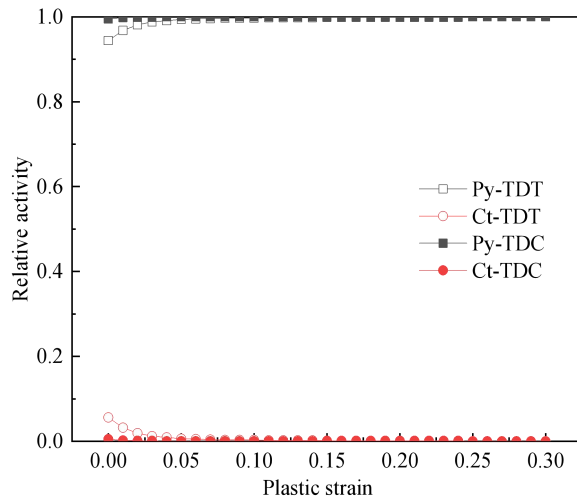
(c) ND   (d) Pole figures

Fig. 22. The role of pyramidal slip and compression twin during plastic deformation.

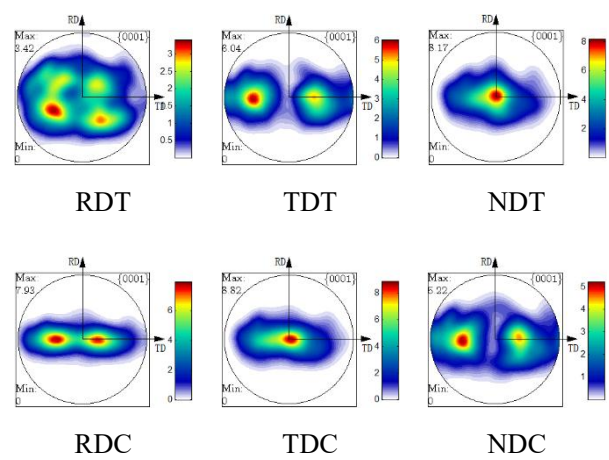For the activation of Pr, Ba and Py, as shown in Fig. 23, the relative activities of deformation modes present the significant anisotropy, initial symmetry and subsequent asymmetry, which account for the same characteristics of flow stress and R-value, as shown in Figs. 17(f) and 18(f). From RD to TD and further to ND, the fraction of Py activity gradually increases and the fraction of Pr activity drops, which make the flow stress go up step by step. Due to the fact that the deformation under RDT, RDC and TDT is dominated by Pr, the texture changes little and presents the bimodal distribution. Overall, for the slip dominated deformation, the pole figures are not changed dramatically, which can be attributed to that the slip make grains rotate gradually.

When Tt and Ct are activated, as shown in Fig. 24, the relative activities of deformation modes shows the significant anisotropy and asymmetry. There are obvious turning region of the relative activity in the strain from 0.05 to 0.1. The same characteristics are also observed in the flow stresses and the plastic flow, as shown in Figs. 17(g) and 18(g). This is a result of the mutual competition and promotion of twin systems. It is worth noting that, for RD and TD, overall the relative activity of Ct is more than that of Tt during tension deformation, while it is opposite during compression. For ND, Tt is easier to be activated in tension, while Ct is in compression. Under the coordination and competition of Tt and Ct, due to the direction dependence of twin and the different rotation of grains, the pole figures present the significant anisotropy and T-C asymmetry, as shown in Fig. 24(d).
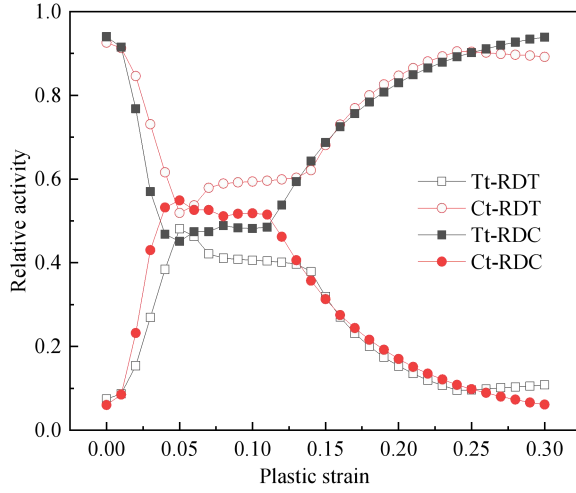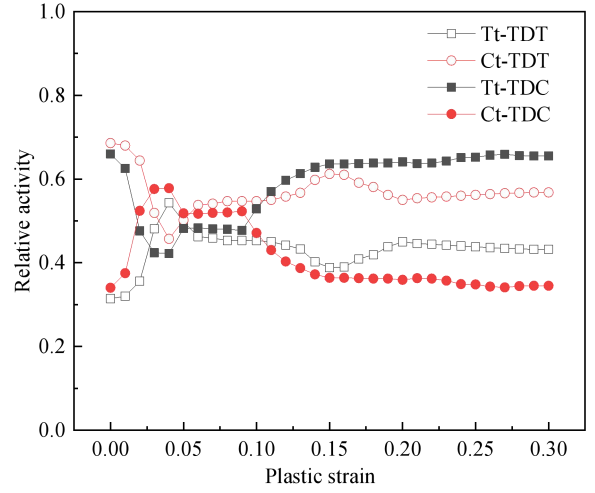

(a) RD   (b) TD

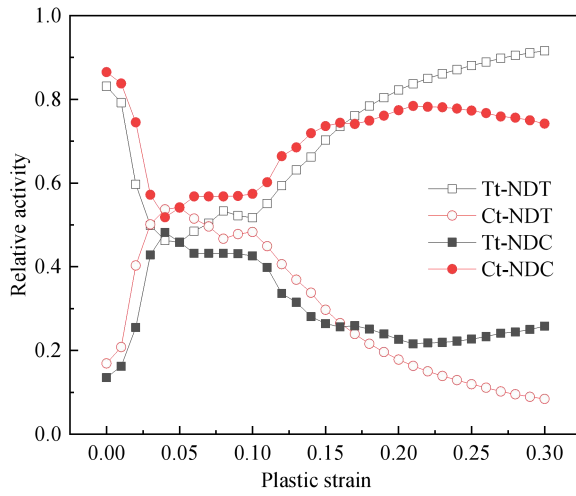(c) ND
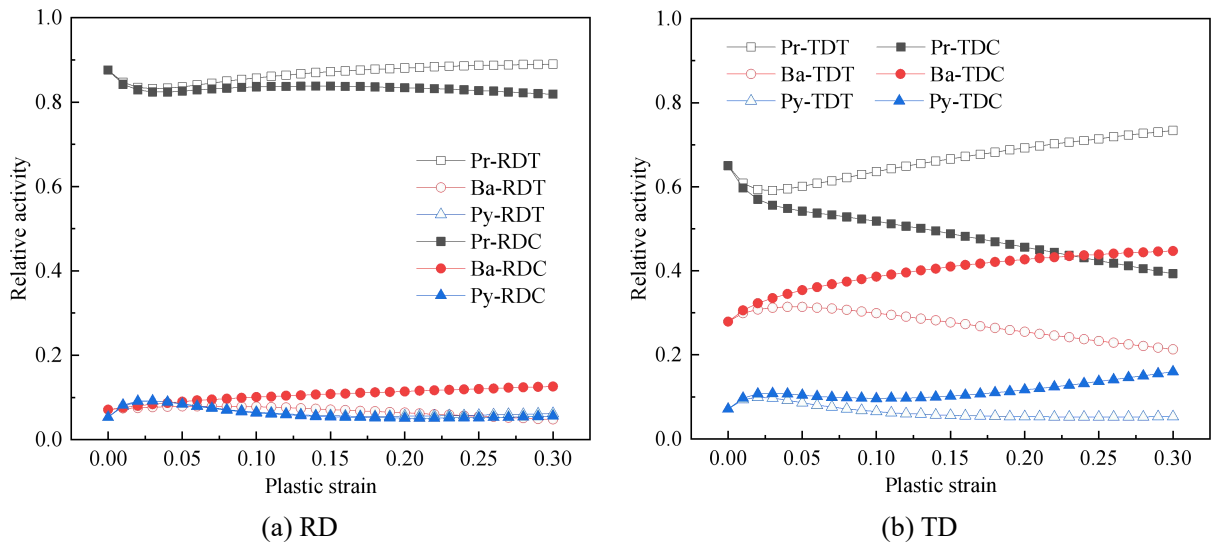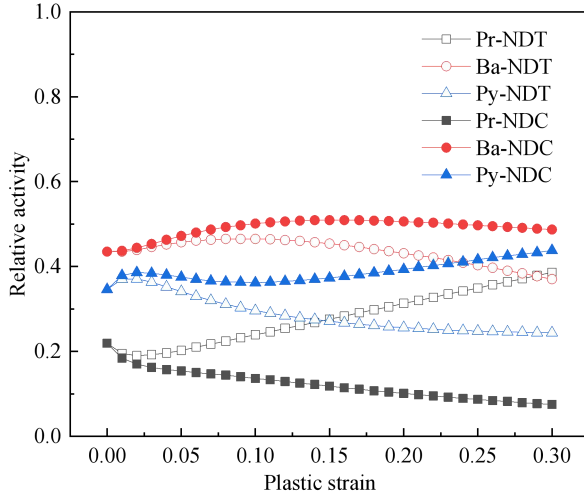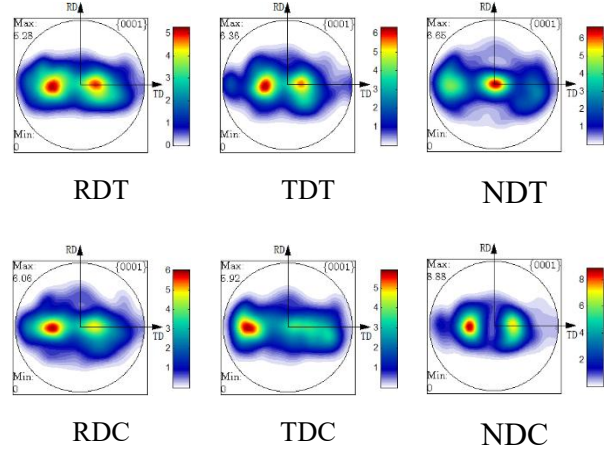
(d) Pole figures

Fig. 23. The role of prismatic, basal and pyramidal slip during plastic deformation.
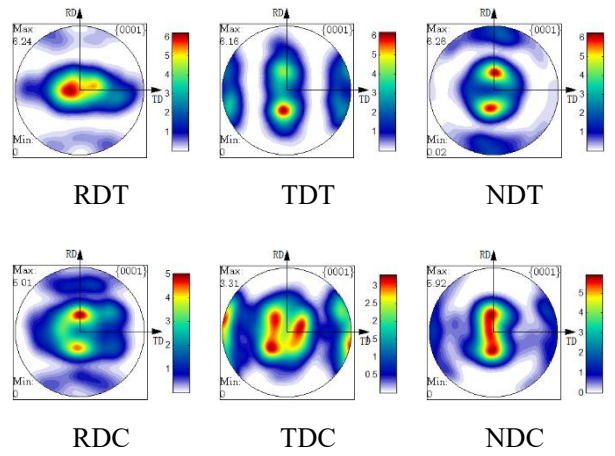

(a) RD

(b) TD

(c) ND

(d) Pole figures

Fig. 24. The role of tension twin and compression twin during plastic deformation.

Above all, the plasticity of materials is determined by the coupling of texture and deformation modes. The relative activities of Pr, Ba, Py, Tt and Ct at the initial stages of deformation are determined by the initial texture and the initial CRSS. Changes in their contributions after some amount of deformation are a result of the coupling between texture evolution and the instantaneous CRSS. The Pr with a smaller CRSS can be easily activated along RD and TD, but Ba mainly coordinates the deformation along TD and ND, and the Py with a larger CRSS is much easier to be activated along ND. Furthermore, Tt is mainly activated in the compression along RD and TD and in the tension along ND, while Ct is opposite. The greater the relative fraction and the CRSS of the activated slip and twin systems are, the larger the flow stress is. For the materials with the c-axes of grains towards to ND, the activation of the slip/twin modes that can coordinate the deformation along the c-axes would reduce the R-value. The direction independence of slip produces the initial T-C symmetry of flow stress and R-value. The difference in the rotation of grains between tension and compression leads to the T-C asymmetry of texture, which in turn causes the asymmetrical evolution of flow stress, R-value and relative activities of deformation modes. The direction dependence of twin would bring about the initial and subsequent T-C asymmetry. The initial texture leads to the difference in the relative activities of slip and twin systems along RD, TD and ND, which is responsible for the anisotropy of flow stress, R-value and deformed texture.

4.3 Modeling of the distorted evolution of anisotropy and asymmetry plasticity

Based on the constructed temperature dependent discontinuous constitutive model, modeling of the distorted evolution of anisotropic and asymmetrical plasticity for α-Ti tube is conducted. The SIM (Yoon's model) is employed to describe the distorted yield loci at different strains and temperatures. The evolution of yield loci with temperature is elaborated and the effect of different deformation modes on yield loci is discussed as follows.

4.3.1 Evolution of yield loci with temperature

Based on the yield stress data obtained from the physical experiments and VPSC-based simulation, the anisotropic coefficients are determined and stated in Appendix A. Fig. 25 shows the evolution of yield loci with strain and temperatures for α-Ti tube. It found that the yield loci by using the Yoon's model match well with the experimental and VPSC data. The distorted evolution of plasticity can be accurately captured by the temperature dependent discontinuous constitutive model. Corresponding to the significant anisotropy and asymmetry of flow stress shown in Fig. 13(a), the yield loci of α-Ti tube at 298K present the remarkably distorted

evolution, as shown in Fig. 25(a). With the increase of temperature, there is a significantly reduced anisotropy and asymmetry in yield loci. At 523K, from Fig. 25(c), an approximate T-C symmetry of yield loci of α-Ti tube is observed. Fig. 25(d) shows that the yield loci of α-Ti tube at large strain present an obvious distorted evolution with temperature. This is attributed to the change of the relative activity of individual deformation modes with the increase of temperature.

(a) Yield loci at 298K   (b) Yield loci at 423K

(c) Yield loci at 523K   (d) Yield loci at the strain of 0.3
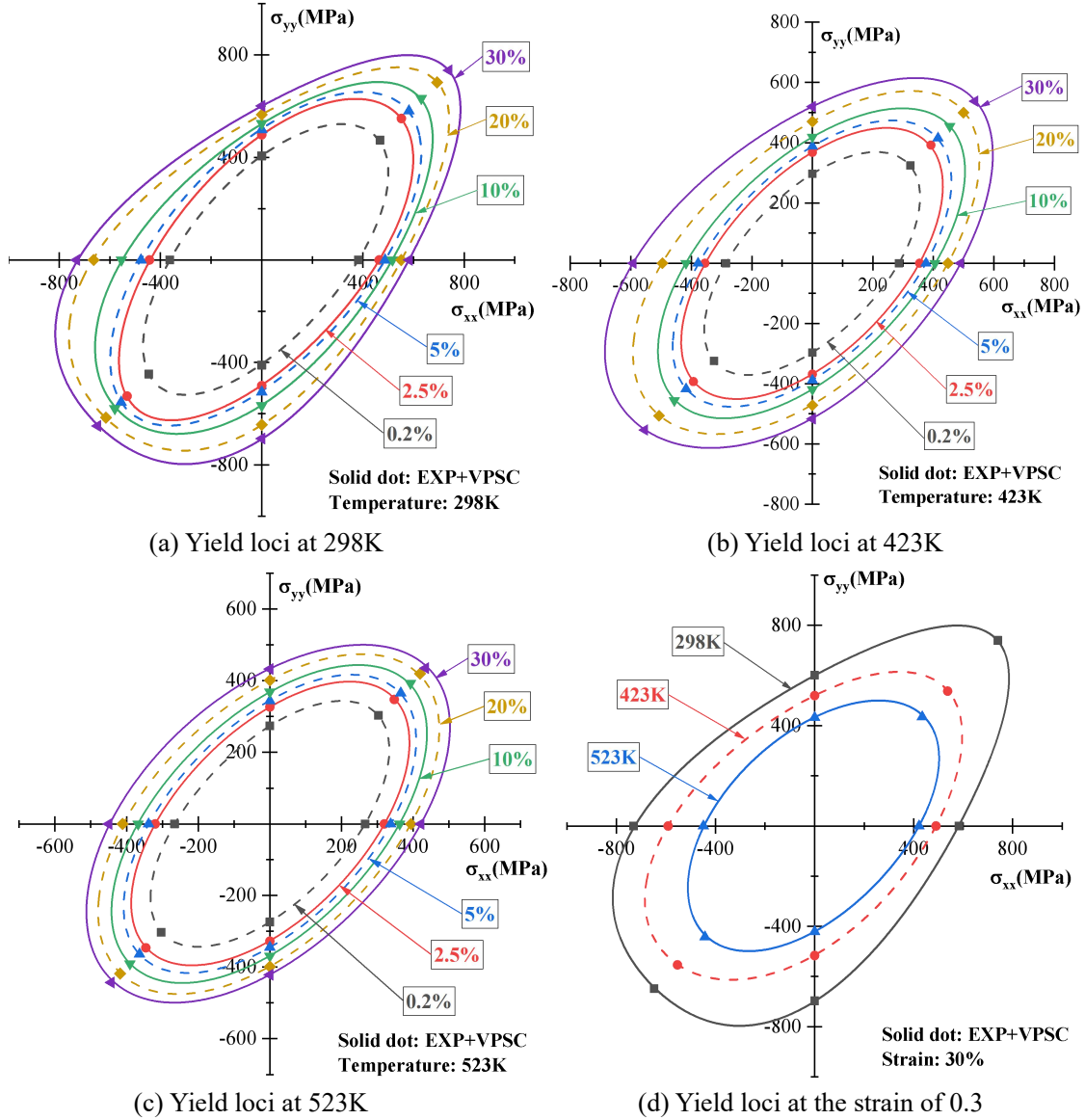
Fig. 25. Evolution of yield loci with temperature and strain for α-Ti tube.

4.3.2 The effect of deformation mechanism on the evolution of yield loci

In order to have a deep understanding of the above evolution characteristics, it is necessary to explore the effect of different deformation mechanisms on yield loci. Thus, based on the yield stress data obtained from the VPSC based simulation, the anisotropic coefficients of α-Ti tube with different deformation mechanisms are determined by the genetic algorithm and stated in

Appendix B. Fig. 26 shows the yield loci of α-Ti tube with different deformation mechanisms. It is found that the distorted evolution of the anisotropy and asymmetry of yield stress can be well captured by the discontinuous constitutive model. For α-Ti tube with different deformation mechanisms, there is an significant differences in the yield behaviors.

Due to the texture effect, a slightly distorted evolution of yield loci is observed when only Py is activated, as shown in Fig. 26(a). For the activation of Pr and Py, from Fig. 26(b), the activity difference of slip systems along different direction also causes distorted yield loci. Fig. 26(c) and (d) shows that the activation of Ba or Tt will lead to an obviously irregular evolution of the anisotropy and asymmetry of yield loci. Due to the less activity of Ct, there is no difference in the yield loci shown in Fig. 26(a) and (e). For the activation of Pr, Ba and Py, from Fig. 26(f), the yield loci present the approximately regular evolution. When only Tt and Ct are activated, as shown in Fig. 26(g), there is an obvious intersection of yield loci due to the alternation of hardening and softening, and a remarkably distorted evolution of anisotropy and asymmetry is observed. Fig. 26(h) shows the comparison of yield loci for α-Ti tube with different deformation mechanisms. It found that the yield loci for α-Ti tube with different deformation mechanisms present significant differences. In general, the activation of Tt or Ct or Ba promotes the irregular evolution of yield loci, while the activation of Pr or Py reduces it.

(a) Py
(b) Py+Pr

(c) Py+Ba

(d) Py+Tw

(e) Py+Cw

(f) Slip

(g) Twin

(h) Comparison of different combinations
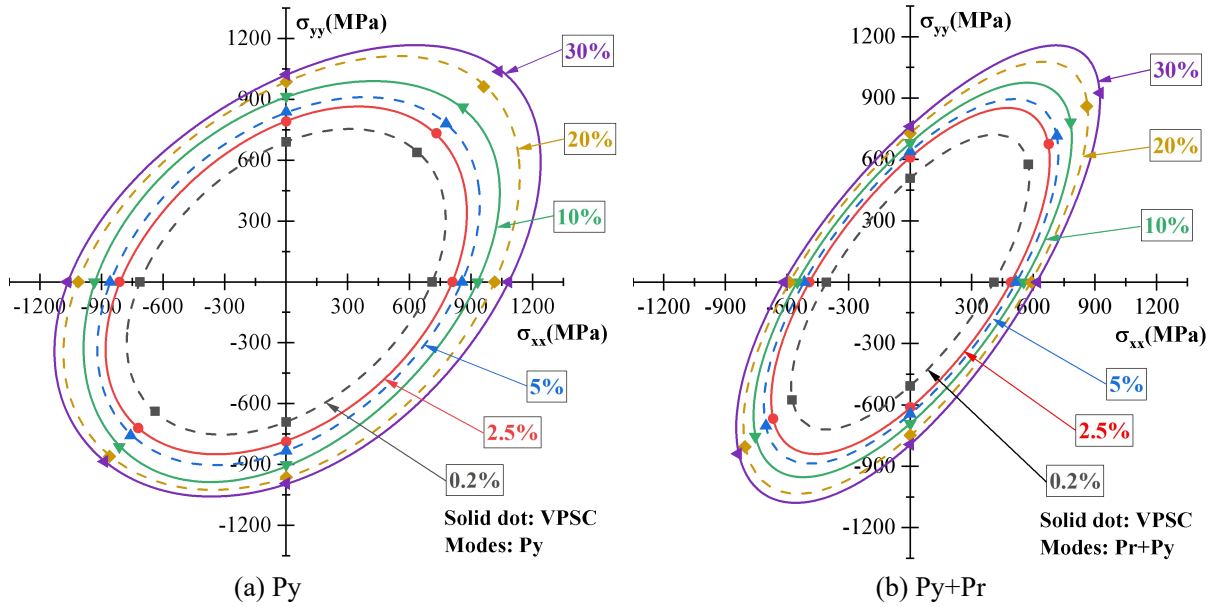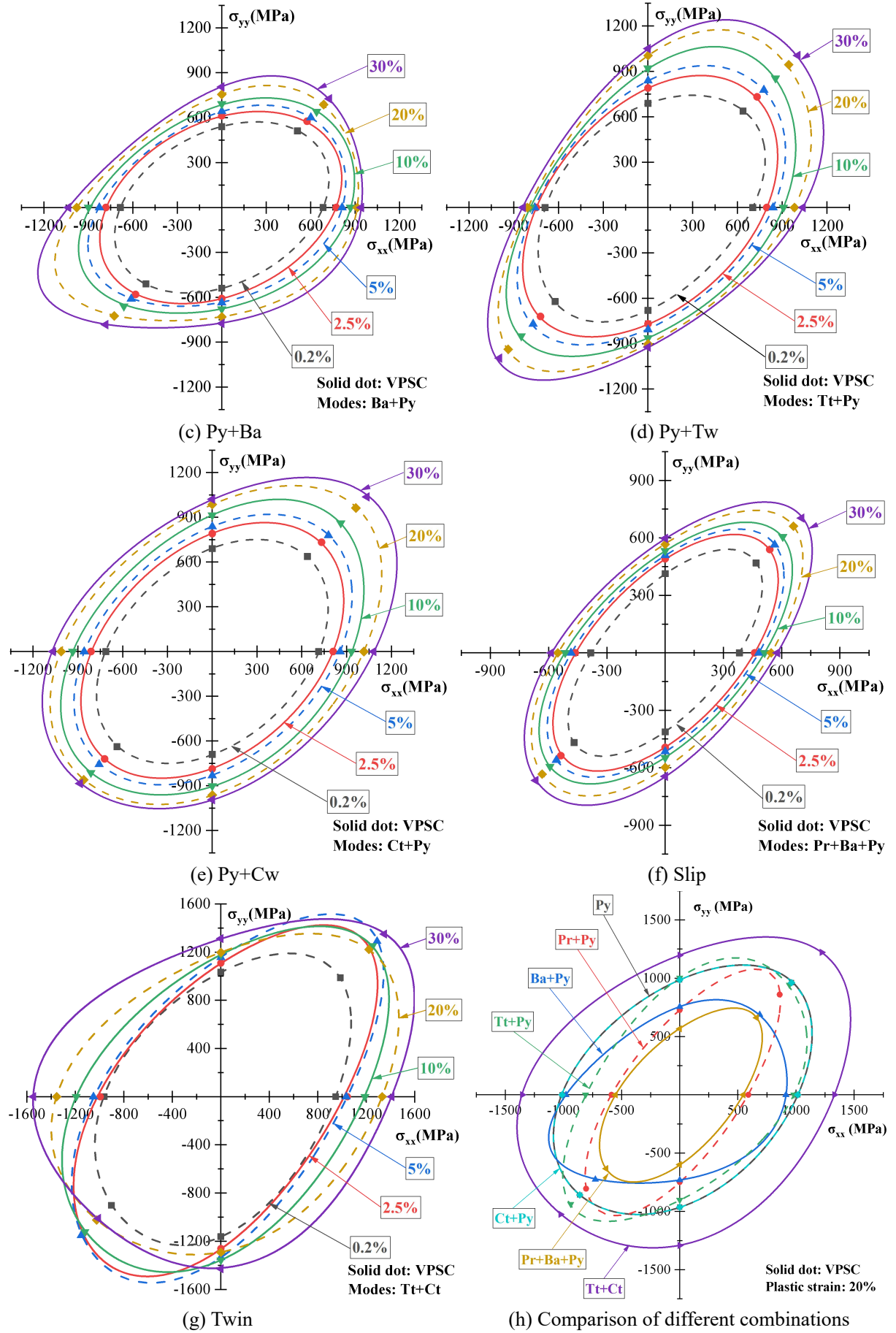
Fig. 26. Evolution of yield loci for the α-Ti tube of different deformation mechanisms.

50

5. Conclusions and remarks

This study presents a general characterization framework to determine the temperature dependent anisotropy and asymmetry of plastic deformation of thin-walled α-Ti materials. The temperature dependent discontinuous constitutive framework is constructed to model the distorted evolution of anisotropy and asymmetry plasticity. The interactive relationship among flow stress, R-value, yield locus, deformation mechanism and texture evolution along different loading directions at different temperatures is analyzed and discussed. The findings are summarized in the following:

(1) By using the HT-DIC system and the designed uniaxial tension/compression specimens, the stress-strain curves and R-values along the RD at different temperatures are obtained. Based on the EBSD analysis on the deformed samples, the slip/twinning dominated multiple mechanisms and the texture evolution with temperature are identified for establishing the VPSC model. Considering the stress-strain curves and the texture evolution during uniaxial tension and compression, the multi-object optimization based method is proposed to calibrate the parameters of the VPSC model for α-Ti tube at different temperatures. Regarding the R-value in uniaxial tension/compression tests and the texture evolution in mandrel bending with inhomogeneous deformation, the calibrated VPSC crystal plasticity model is thoroughly validated.

(2) The α-Ti tube shows the significant anisotropy and T-C asymmetry in flow stress and R-value at 298K. The increase of temperature promotes the activity of slip and suppresses the activity of Tt, and then leads to the significantly reduced anisotropy and asymmetry. The larger fraction of Tt makes the texture change drastically at room temperature, the reduction of Tt activity with temperature increasing decreases the change of texture. The texture evolution is insensitive to temperature for the slip dominated deformation.

(3) The anisotropy and asymmetry of plasticity are a result of the coupling between texture evolution and the activity difference of Pr, Ba, Py, Tt and Ct. The activation of slip systems produces the initial T-C symmetry of flow stress and R-value and then the discrepant rotation of grains between tension and compression causes the asymmetric evolution of flow stress, R-value, texture and relative activities of individual deformation modes. The twinning leads to the initial asymmetry and the subsequent asymmetric evolution. The greater fraction of activated deformation mode with a high CRSS would cause a larger flow stress. The activation of the slip/twin modes that can coordinate the deformation along the c-axes would reduce the R-value of the materials that the c-axes of grains is towards to ND.

(4) For α-Ti tube at 298K, the activation of Tt leads to the significant distorted evolution of anisotropy and asymmetry of yield loci, but the evolution of yield loci is close to isotropy at 523K because the increasing of temperature suppresses the activity of twin. At a large strain, the yield loci of α-Ti tube present an obvious distorted evolution with temperature. The coupling between the texture evolution of materials and the activity difference of slip and twin systems leads to distorted yield loci. The activation of Tt or Ct or Ba promotes the irregular evolution of yield loci, while the activation of Pr or Py reduces it.

Acknowledgements

Appendix A. Material parameters of α-Ti tube at different temperatures

Table A-1 Anisotropic coefficients of α-Ti tube at 298K for SIM (Yoon's mode).

$\bar{\varepsilon}^p$	a_1	a_2	a_3	a_4	b_1	b_2	b_3	b_4
0.2%	1.287	1.609	1.944	1.784	-0.460	1.701	0.585	0.434
2.5%	1.335	1.623	1.930	1.797	-0.427	1.635	0.618	0.460
5.0%	1.382	1.592	1.903	1.795	-0.291	2.094	0.180	-0.360
10%	1.435	1.535	1.816	1.775	-0.988	-1.069	-1.081	-0.782
20%	1.457	1.474	1.714	1.708	-0.974	-1.295	-1.579	1.250
30%	1.462	1.476	1.678	1.657	-1.031	-1.342	-1.645	-1.350

Table A-2 Anisotropic coefficients of α-Ti tube at 423K for SIM (Yoon's mode).

$\bar{\varepsilon}^p$	a_1	a_2	a_3	a_4	b_1	b_2	b_3	b_4
0.2%	1.457	1.595	1.866	1.795	0.481	0.511	0.000	-0.166
2.5%	1.499	1.635	1.827	1.761	0.250	0.923	0.002	-0.160
5.0%	1.515	1.620	1.842	1.761	0.770	0.323	0.000	-0.166
10%	1.521	1.574	1.834	1.778	-0.001	-0.432	-1.423	0.903
20%	1.539	1.541	1.758	1.748	0.095	-1.660	-0.865	-0.641
30%	1.600	1.507	1.683	1.691	1.092	-1.555	-1.318	1.332

Table A-3 Anisotropic coefficients of α-Ti tube at 523K for SIM (Yoon's mode).

$\bar{\varepsilon}^p$	a_1	a_2	a_3	a_4	b_1	b_2	b_3	b_4
0.2%	1.467	1.572	1.888	1.820	0.037	-0.037	0.000	0.000
2.5%	1.562	1.631	1.831	1.775	-0.411	-0.662	0.000	0.174
5.0%	1.570	1.637	1.824	1.773	0.037	-0.037	0.000	0.000
10%	1.585	1.621	1.808	1.772	0.000	-0.381	-1.253	0.000
20%	1.641	1.627	1.771	1.764	0.083	-0.279	-2.181	0.000
30%	1.689	1.643	1.726	1.742	0.273	-0.388	-2.180	0.000

Appendix B. Material parameters of α-Ti tube with different deformation mechanisms

Table B-1 Anisotropic coefficients of α-Ti tube when Py is activated.

$\bar{\varepsilon}^p$	a_1	a_2	a_3	a_4	b_1	b_2	b_3	b_4
0.2%	1.271	1.598	1.915	1.755	-0.742	1.000	0.742	0.000
2.5%	1.231	1.538	1.936	1.790	0.214	-2.264	0.082	0.000
5.0%	1.237	1.477	1.959	1.808	-1.670	1.486	-0.123	1.246
10%	1.307	1.430	1.941	1.838	-0.185	-0.836	1.958	0.850
20%	1.434	1.384	1.859	1.819	-0.424	-1.096	-1.578	1.103
30%	1.478	1.373	1.774	1.783	-0.348	-1.087	-1.977	1.200

Table B-2 Anisotropic coefficients of α-Ti tube when Py and Pr are activated.

$\bar{\varepsilon}^p$	a_1	a_2	a_3	a_4	b_1	b_2	b_3	b_4
0.2%	1.271	1.598	1.915	1.755	-0.742	1.000	0.742	0.000
2.5%	1.231	1.538	1.936	1.790	0.214	-2.264	0.082	0.000
5.0%	1.237	1.477	1.959	1.808	-1.670	1.486	-0.123	1.246
10%	1.307	1.430	1.941	1.838	-0.185	-0.836	1.958	0.850
20%	1.434	1.384	1.859	1.819	-0.424	-1.096	-1.578	1.103
30%	1.478	1.373	1.774	1.783	-0.348	-1.087	-1.977	1.200

Table B-3 Anisotropic coefficients of α-Ti tube when Py and Ba are activated.

$\bar{\varepsilon}^p$	a_1	a_2	a_3	a_4	b_1	b_2	b_3	b_4
0.2%	1.271	1.598	1.915	1.755	-0.742	1.000	0.742	0.000
2.5%	1.231	1.538	1.936	1.790	0.214	-2.264	0.082	0.000
5.0%	1.237	1.477	1.959	1.808	-1.670	1.486	-0.123	1.246
10%	1.307	1.430	1.941	1.838	-0.185	-0.836	1.958	0.850
20%	1.434	1.384	1.859	1.819	-0.424	-1.096	-1.578	1.103
30%	1.478	1.373	1.774	1.783	-0.348	-1.087	-1.977	1.200

Table B-4 Anisotropic coefficients of α-Ti tube when Py and Tt are activated.

$\bar{\varepsilon}^p$	a_1	a_2	a_3	a_4	b_1	b_2	b_3	b_4

$\overline{\varepsilon}^p$	a_1	a_2	a_3	a_4	b_1	b_2	b_3	b_4
0.2%	1.271	1.598	1.915	1.755	-0.742	1.000	0.742	0.000
2.5%	1.231	1.538	1.936	1.790	0.214	-2.264	0.082	0.000
5.0%	1.237	1.477	1.959	1.808	-1.670	1.486	-0.123	1.246
10%	1.307	1.430	1.941	1.838	-0.185	-0.836	1.958	0.850
20%	1.434	1.384	1.859	1.819	-0.424	-1.096	-1.578	1.103
30%	1.478	1.373	1.774	1.783	-0.348	-1.087	-1.977	1.200

Table B-5 Anisotropic coefficients of α-Ti tube when Py and Ct are activated.

$\overline{\varepsilon}^p$	a_1	a_2	a_3	a_4	b_1	b_2	b_3	b_4
0.2%	1.271	1.598	1.915	1.755	-0.742	1.000	0.742	0.000
2.5%	1.231	1.538	1.936	1.790	0.214	-2.264	0.082	0.000
5.0%	1.237	1.477	1.959	1.808	-1.670	1.486	-0.123	1.246
10%	1.307	1.430	1.941	1.838	-0.185	-0.836	1.958	0.850
20%	1.434	1.384	1.859	1.819	-0.424	-1.096	-1.578	1.103
30%	1.478	1.373	1.774	1.783	-0.348	-1.087	-1.977	1.200

Table B-6 Anisotropic coefficients of α-Ti tube when Pr, Ba and Py are activated.

$\overline{\varepsilon}^p$	a_1	a_2	a_3	a_4	b_1	b_2	b_3	b_4
0.2%	1.271	1.598	1.915	1.755	-0.742	1.000	0.742	0.000
2.5%	1.231	1.538	1.936	1.790	0.214	-2.264	0.082	0.000
5.0%	1.237	1.477	1.959	1.808	-1.670	1.486	-0.123	1.246
10%	1.307	1.430	1.941	1.838	-0.185	-0.836	1.958	0.850
20%	1.434	1.384	1.859	1.819	-0.424	-1.096	-1.578	1.103
30%	1.478	1.373	1.774	1.783	-0.348	-1.087	-1.977	1.200

Table B-7 Anisotropic coefficients of α-Ti tube when Tt and Ct are activated.

$\overline{\varepsilon}^p$	a_1	a_2	a_3	a_4	b_1	b_2	b_3	b_4
0.2%	1.271	1.598	1.915	1.755	-0.742	1.000	0.742	0.000
2.5%	1.231	1.538	1.936	1.790	0.214	-2.264	0.082	0.000
5.0%	1.237	1.477	1.959	1.808	-1.670	1.486	-0.123	1.246
10%	1.307	1.430	1.941	1.838	-0.185	-0.836	1.958	0.850
20%	1.434	1.384	1.859	1.819	-0.424	-1.096	-1.578	1.103
30%	1.478	1.373	1.774	1.783	-0.348	-1.087	-1.977	1.200

References

Ahn, K., Huh, H., Yoon, J., 2015. Rate-dependent hardening model for pure titanium considering the effect of deformation twinning. Int. J. Mech. Sci. 98, 80–92. https://doi.org/10.1016/j.ijmecsci.2015.04.008

Banabic, D., 2010. Sheet Metal Forming Processes, Springer. Springer Berlin Heidelberg, Berlin, Heidelberg. https://doi.org/10.1007/978-3-540-88113-1

Baral, M., Hama, T., Knudsen, E., Korkolis, Y.P., 2018. Plastic deformation of commercially-pure titanium: Experiments and modeling. Int. J. Plast. 105, 164–194. https://doi.org/10.1016/J.IJPLAS.2018.02.009

Barlat, F., Aretz, H., Yoon, J.W., Karabin, M.E., Brem, J.C., Dick, R.E., 2005. Linear transfomation-based anisotropic yield functions. Int. J. Plast. 21, 1009–1039. https://doi.org/10.1016/j.ijplas.2004.06.004

Bennett, C.J., Leen, S.B., Williams, E.J., Shipway, P.H., Hyde, T.H., 2010. A critical analysis of plastic flow behaviour in axisymmetric isothermal and Gleeble compression testing. Comput. Mater. Sci. 50, 125–137. https://doi.org/10.1016/j.commatsci.2010.07.016

Bishoyi, B.D., Sabat, R.K., Sahu, J., Sahoo, S.K., 2017. Effect of Temperature on Microstructure and Texture Evolution during Uniaxial Tension of Commercially Pure Titanium. Mater. Sci. Eng. A 703, 399–412. https://doi.org/10.1016/j.msea.2017.07.081

Cao, J., Lee, W., Cheng, H.S., Seniw, M., Wang, H.P., Chung, K., 2009. Experimental and numerical investigation of combined isotropic-kinematic hardening behavior of sheet metals. Int. J. Plast. 25, 942–972. https://doi.org/10.1016/j.ijplas.2008.04.007

Cazacu, O., Plunkett, B., Barlat, F., 2006. Orthotropic yield criterion for hexagonal closed packed metals. Int. J. Plast. 22, 1171–1194. https://doi.org/10.1016/j.ijplas.2005.06.001

Chichili, D.R., Ramesh, K.T., Hemker, K.J., 1998. The high-strain-rate response of alpha-titanium: Experiments, deformation mechanisms and modeling. Acta Mater. 46, 1025–1043. https://doi.org/10.1016/S1359-6454(97)00287-5

Chun, Y.B., Yu, S.H., Semiatin, S.L., Hwang, S.K., 2005. Effect of deformation twinning on microstructure and texture evolution during cold rolling of CP-titanium. Mater. Sci. Eng. A 398, 209–219. https://doi.org/10.1016/j.msea.2005.03.019

Cui, X.L., Yuan, S.J., 2016. Determination of mechanical properties of anisotropic thin-walled tubes under three-dimensional stress state. Int. J. Adv. Manuf. Technol. 87, 1917–1927. https://doi.org/10.1007/s00170-016-8526-3

Djavanroodi, F., Janbakhsh, M., 2013. Formability Characterization of Titanium Alloy Sheets, in: Sieniawski, J. (Ed.), Titanium Alloys - Advances in Properties Control. InTech, pp. 299–365. https://doi.org/10.5772/55889

Gatea, S., Xu, D., Ou, H., McCartney, G., 2018. Evaluation of formability and fracture of pure titanium in incremental sheet forming. Int. J. Adv. Manuf. Technol. 95, 625–641. https://doi.org/10.1007/s00170-017-1195-z

Ghaffari Tari, D., Worswick, M.J., Ali, U., Gharghouri, M.A., 2014. Mechanical response of AZ31B magnesium alloy: Experimental characterization and material modeling considering proportional loading at room temperature. Int. J. Plast. 55, 247–267. https://doi.org/10.1016/j.ijplas.2013.10.006

Gurao, N.P., Kapoor, R., Suwas, S., 2011. Deformation behaviour of commercially pure titanium at extreme strain rates. Acta Mater. 59, 3431–3446. https://doi.org/10.1016/j.actamat.2011.02.018

Hama, T., Kobuki, A., Takuda, H., 2017. Crystal-plasticity finite-element analysis of anisotropic deformation behavior in a commercially pure titanium Grade 1 sheet. Int. J. Plast. 91, 77–108. https://doi.org/10.1016/j.ijplas.2016.12.005

Hama, T., Nagao, H., Kobuki, A., Fujimoto, H., Takuda, H., 2014. Work-hardening and twinning behaviors in a commercially pure titanium sheet under various loading paths. Mater. Sci. Eng. A 620, 390–398. https://doi.org/10.1016/j.msea.2014.10.024

He, Z., Yuan, S., Lin, Y., Wang, X., Hu, W., 2014. Analytical model for tube hydro-bulging test, part I: Models for stress components and bulging zone profile. Int. J. Mech. Sci. 87, 297–306. https://doi.org/10.1016/j.ijmecsci.2014.05.009

He, Z., Yuan, S., Liu, G., Wu, J., Cha, W., 2010. Formability testing of AZ31B magnesium alloy tube at elevated temperature. J. Mater. Process. Technol. 210, 877–884. https://doi.org/10.1016/j.jmatprotec.2010.01.020

Hill, R., 1948. A Theory of the Yielding and Plastic Flow of Anisotropic Metals. Proc. R. Soc. London A Math. Phys. Eng. Sci. 193, 281–297. https://doi.org/10.1098/rspa.1948.0045

Huang, W., Zan, X., Nie, X., Gong, M., Wang, Y., Xia, Y., 2007. Experimental study on the dynamic tensile behavior of a poly-crystal pure titanium at elevated temperatures. Mater. Sci. Eng. A 443, 33–41. https://doi.org/10.1016/j.msea.2006.06.041

Jiang, L., Jonas, J.J., Boyle, K., Martin, P., 2008. Deformation behavior of two Mg alloys during ring hoop tension testing. Mater. Sci. Eng. A 492, 68–73. https://doi.org/10.1016/j.msea.2008.04.028

Karbasian, H., Tekkaya, A.E., 2010. A review on hot stamping. J. Mater. Process. Technol. 210, 2103–2118. https://doi.org/10.1016/j.jmatprotec.2010.07.019

Kitamura, K., Terano, M., 2014. Determination of local properties of plastic anisotropy in thick plate by small-cube compression test for precise simulation of plate forging. CIRP Ann. 63, 293–296. https://doi.org/10.1016/j.cirp.2014.03.038

Knezevic, M., Lebensohn, R.A., Cazacu, O., Revil-Baudard, B., Proust, G., Vogel, S.C., Nixon, M.E., 2013. Modeling bending of α-titanium with embedded polycrystal plasticity in implicit finite elements. Mater. Sci. Eng. A 564, 116–126. https://doi.org/10.1016/j.msea.2012.11.037

Lee, M.-G., Barlat, F., 2014. Modeling of Plastic Yielding, Anisotropic Flow, and the Bauschinger Effect, in: Comprehensive Materials Processing. Elsevier, pp. 235–260. https://doi.org/10.1016/B978-0-08-096532-1.00219-3

Li, H., Hu, X., Yang, H., Li, L., 2016. Anisotropic and asymmetrical yielding and its distorted evolution: Modeling and applications. Int. J. Plast. 82, 127–158. https://doi.org/10.1016/j.ijplas.2016.03.002

Li, H., Ma, J., Liu, B.Y., Gu, R.J., Li, G.J., 2018. An insight into neutral layer shifting in tube bending. Int. J. Mach. Tools Manuf. 126, 51–70. https://doi.org/10.1016/j.ijmachtools.2017.11.013

Li, H., Zhang, H.Q., Yang, H., Fu, M.W., Yang, Heng, 2017. Anisotropic and asymmetrical yielding and its evolution in plastic deformation: Titanium tubular materials. Int. J. Plast. 90, 177–211. https://doi.org/10.1016/j.ijplas.2017.01.004

Lin, P., Hao, Y., Zhang, B., Zhang, S., Chi, C., Shen, J., 2017. Tension-Compression Asymmetry in Yielding and Strain Hardening Behavior of CP-Ti at Room Temperature. Mater. Sci. Eng. A 707, 172–180. https://doi.org/10.1016/j.msea.2017.09.042

Liu, J., Li, J., Dirras, G., Ameyama, K., Cazes, F., Ota, M., 2018. A three-dimensional multi-scale polycrystalline plasticity model coupled with damage for pure Ti with harmonic structure design. Int. J. Plast. 100, 192–207. https://doi.org/10.1016/j.ijplas.2017.10.006

Martínez, A., Miguel, V., Coello, J., Manjabacas, M.C., 2017. Determining stress distribution by tension and by compression applied to steel: Special analysis for TRIP steel sheets. Mater. Des. 125, 11–25. https://doi.org/10.1016/j.matdes.2017.03.079

Mayama, T., Aizawa, K., Tadano, Y., Kuroda, M., 2009. Influence of twinning deformation and lattice rotation on strength differential effect in polycrystalline pure magnesium with rolling texture. Comput. Mater. Sci. 47, 448–455. https://doi.org/10.1016/j.commatsci.2009.09.009

Nemat-Nasser, S., Guo, W.G., Cheng, J.Y., 1999. Mechanical properties and deformation mechanisms of a commercially pure titanium. Acta Mater. 47, 3705–3720. https://doi.org/10.1016/S1359-6454(99)00203-7

Nie, D., Lu, Z., Zhang, K., 2018. Hot V-bending behavior of pre-deformed pure titanium sheet assisted by electrical heating. Int. J. Adv. Manuf. Technol. 94, 163–174. https://doi.org/10.1007/s00170-017-0632-3

Nixon, M.E., Cazacu, O., Lebensohn, R.A., 2010a. Anisotropic response of high-purity α-titanium: Experimental characterization and constitutive modeling. Int. J. Plast. 26, 516–532. https://doi.org/10.1016/j.ijplas.2009.08.007

Nixon, M.E., Lebensohn, R.A., Cazacu, O., Liu, C., 2010b. Experimental and finite-element analysis of the anisotropic response of high-purity α-titanium in bending. Acta Mater. 58, 5759–5767. https://doi.org/10.1016/j.actamat.2010.06.051

Orozco-Caballero, A., Li, F., Esqué-de los Ojos, D., Atkinson, M.D., Quinta da Fonseca, J., 2018. On the ductility of alpha titanium: The effect of temperature and deformation mode. Acta Mater. 149, 1–10. https://doi.org/10.1016/j.actamat.2018.02.022

Panda, S., Sahoo, S.K., Dash, A., Bagwan, M., Kumar, G., Mishra, S.C., Suwas, S., 2014. Orientation dependent mechanical properties of commercially pure (cp) titanium. Mater. Charact. 98, 93–101. https://doi.org/10.1016/j.matchar.2014.10.011

Plunkett, B., Cazacu, O., Barlat, F., 2008. Orthotropic yield criteria for description of the anisotropy in tension and compression of sheet metals. Int. J. Plast. 24, 847–866. https://doi.org/10.1016/j.ijplas.2007.07.013

Qin, H., Jonas, J.J., Yu, H., Brodusch, N., Gauvin, R., Zhang, X., 2014. Initiation and accommodation of primary twins in high-purity titanium. Acta Mater. 71, 293–305. https://doi.org/10.1016/j.actamat.2014.03.025

Raemy, C., Manopulo, N., Hora, P., 2017. On the modelling of plastic anisotropy, asymmetry and directional hardening of commercially pure titanium: A planar Fourier series based approach. Int. J. Plast. 91, 182–204. https://doi.org/10.1016/j.ijplas.2017.02.010

Rawat, S., Mitra, N., 2018. Molecular dynamics investigation of c-axis deformation of single crystal Ti under uniaxial stress conditions: Evolution of compression twinning and dislocations. Comput. Mater. Sci. 141, 19–29. https://doi.org/10.1016/j.commatsci.2017.09.015

SAE, 2010. Titanium Tubing, Welded Annealed, 40 ksi (276 MPa) Yield Strength. AMS G Titan. Refract. Met. Comm. AMS4941E. https://doi.org/http://doi.org/10.4271/AMS4941E

Sahoo, S.K., Sabat, R.K., Sahni, S., Suwas, S., 2016. Texture and microstructure evolution of commercially pure titanium during hot rolling: Role of strain-paths. Mater. Des. 91, 58–71. https://doi.org/10.1016/j.matdes.2015.11.073

Shutov, A. V., Ihlemann, J., 2012. A viscoplasticity model with an enhanced control of the yield surface distortion. Int. J. Plast. 39, 152–167. https://doi.org/10.1016/j.ijplas.2012.06.006

Singh, A., Basak, S., Lin, L.P., Roy, G.G., Jha, M.N., Mascarenhas, M., Panda, S.K., 2018. Prediction of earing defect and deep drawing behavior of commercially pure titanium sheets using CPB06 anisotropy yield theory. J. Manuf. Process. 33, 256–267. https://doi.org/10.1016/j.jmapro.2018.05.003

Smith, J., Liu, W.K., Cao, J., 2015. A general anisotropic yield criterion for pressure-dependent materials. Int. J. Plast. 75, 2–21. https://doi.org/10.1016/j.ijplas.2015.08.009

Suwas, S., Beausir, B., T??th, L.S., Fundenberger, J.J., Gottstein, G., 2011. Texture evolution in commercially pure titanium after warm equal channel angular extrusion. Acta Mater. 59, 1121–1133. https://doi.org/10.1016/j.actamat.2010.10.045

Tekkaya, A.E., Allwood, J.M., Bariani, P.F., Bruschi, S., Cao, J., Gramlich, S., Groche, P., Hirt, G., Ishikawa, T., Löbbe, C., Lueg-Althoff, J., Merklein, M., Misiolek, W.Z., Pietrzyk, M., Shivpuri, R., Yanagimoto, J., 2015. Metal forming beyond shaping: Predicting and setting product properties. CIRP Ann. 64, 629–653. https://doi.org/10.1016/j.cirp.2015.05.001

Tirry, W., Bouvier, S., Benmhenni, N., Hammami, W., Habraken, A.M., Coghe, F., Schryvers, D., Rabet, L., 2012. Twinning in pure Ti subjected to monotonic simple shear deformation. Mater. Charact. 72, 24–36. https://doi.org/10.1016/j.matchar.2012.07.001

Tomé, C.N., Lebensohn, R.A., Kocks, U.F., 1991. A model for texture development dominated by deformation twinning: Application to zirconium alloys. Acta Metall. Mater. 39, 2667–2680. https://doi.org/10.1016/0956-7151(91)90083-D

Tsao, L.C., Wu, H.Y., Leong, J.C., Fang, C.J., 2012. Flow stress behavior of commercial pure titanium sheet during warm tensile deformation. Mater. Des. 34, 179–184. https://doi.org/10.1016/j.matdes.2011.07.060

Tuninetti, V., Gilles, G., Milis, O., Pardoen, T., Habraken, A.M., 2015. Anisotropy and tension-compression asymmetry modeling of the room temperature plastic response of Ti-6Al-4V. Int. J. Plast. 67, 53–68. https://doi.org/10.1016/j.ijplas.2014.10.003

ul Hassan, H., Maqbool, F., Güner, A., Hartmaier, A., Ben Khalifa, N., Tekkaya, A.E., 2016. Springback prediction and reduction in deep drawing under influence of unloading modulus degradation. Int. J. Mater. Form. 9, 619–633. https://doi.org/10.1007/s12289-015-1248-5

Ungár, T., Glavicic, M.G., Balogh, L., Nyilas, K., Salem, A.A., Ribárik, G., Semiatin, S.L., 2008. The use of X-ray diffraction to determine slip and twinning activity in commercial-purity (CP) titanium. Mater. Sci. Eng. A 493, 79–85. https://doi.org/10.1016/j.msea.2007.06.096

Venugopal, S., Venugopal, P., Mannan, S.L., 2008. Optimisation of cold and warm workability of commercially pure titanium using dynamic materials model (DMM) instability maps. J. Mater. Process. Technol. 202, 201–215. https://doi.org/10.1016/j.jmatprotec.2007.09.038

Wang, H., Wu, P., Zhou, G., Li, D., Li, Z., Peng, Y., 2018. Misorientation development in continuous dynamic recrystallization of AZ31B alloy sheet and polycrystal plasticity simulation. Mater. Sci. Eng. A 730, 438–456. https://doi.org/10.1016/j.msea.2018.05.095

Warwick, J.L.W., Jones, N.G., Rahman, K.M., Dye, D., 2012. Lattice strain evolution during tensile and compressive loading of CP Ti. Acta Mater. 60, 6720–6731. https://doi.org/10.1016/j.actamat.2012.08.042

Williams, B.W., Boyle, K.P., 2016. Characterization of anisotropic yield surfaces for titanium sheet using hydrostatic bulging with elliptical dies. Int. J. Mech. Sci. 114, 315–329. https://doi.org/10.1016/j.ijmecsci.2016.05.022

Williams, J.C., Baggerly, R.G., Paton, N.E., 2002. Deformation behavior of HCP Ti-Al alloy single crystals. Metall. Mater. Trans. A 33, 837–850. https://doi.org/10.1007/s11661-002-1016-2

Wronski, M., Kumar, M.A., Capolungo, L., McCabe, R.J., Wierzbanowski, K., Tomé, C.N., 2018. Deformation behavior of CP-titanium: Experiment and Crystal plasticity modeling. Mater. Sci. Eng. A 724, 289–297. https://doi.org/10.1016/j.msea.2018.03.017

Xu, S., Toth, L.S., Schuman, C., Lecomte, J.S., Barnett, M.R., 2017. Dislocation mediated variant selection for secondary twinning in compression of pure titanium. Acta Mater. 124, 59–70. https://doi.org/10.1016/j.actamat.2016.10.063

Yang, H., Li, H., Ma, J., Zhang, Z., Chen, J., 2019. Constitutive modeling related uncertainties: Effects on deformation prediction accuracy of sheet metallic materials. Int. J. Mech. Sci. 157–158, 574–598. https://doi.org/10.1016/j.ijmecsci.2019.05.004

Yi, N., Hama, T., Kobuki, A., Fujimoto, H., Takuda, H., 2016. Anisotropic deformation behavior under various strain paths in commercially pure titanium Grade 1 and Grade 2 sheets. Mater. Sci. Eng. A 655, 70–85. https://doi.org/10.1016/j.msea.2015.12.081

Yoo, M.H., 1981. Slip, twinning, and fracture in hexagonal close-packed metals. Metall. Trans. A 12, 409–418. https://doi.org/10.1007/BF02648537

Yoon, J.W., Lou, Y., Yoon, J., Glazoff, M. V., 2014. Asymmetric yield function based on the stress invariants for pressure sensitive metals. Int. J. Plast. 56, 184–202. https://doi.org/10.1016/j.ijplas.2013.11.008

Zeng, Z., Jonsson, S., Roven, H.J., 2009a. The effects of deformation conditions on microstructure and texture of commercially pure Ti. Acta Mater. 57, 5822–5833. https://doi.org/10.1016/j.actamat.2009.08.016

Zeng, Z., Zhang, Y., Jonsson, S., 2009b. Deformation behaviour of commercially pure titanium during simple hot compression. Mater. Des. 30, 3105–3111. https://doi.org/10.1016/j.matdes.2008.12.002

Zeng, Z., Zhang, Y., Jonsson, S., 2009c. Microstructure and texture evolution of commercial pure titanium deformed at elevated temperatures. Mater. Sci. Eng. A 513–514, 83–90. https://doi.org/10.1016/j.msea.2009.01.065

Zhai, J., Luo, T., Gao, X., Graham, S.M., Baral, M., Korkolis, Y.P., Knudsen, E., 2016. Modeling the ductile damage process in commercially pure titanium. Int. J. Solids Struct. 91, 26–45. https://doi.org/10.1016/j.ijsolstr.2016.04.031

Zhang, X., Yang, H., Li, H., Zhang, Z., Li, L., 2014. Warm bending mechanism of extrados and intrados of large diameter thin-walled CP-Ti tubes. Trans. Nonferrous Met. Soc. China 24, 3257–3264. https://doi.org/10.1016/S1003-6326(14)63465-8

Zhang, Z., Yang, H., Li, H., Tao, Z., Wang, D., 2014. Thermo-mechanical coupled 3D-FE modeling of heat rotary draw bending for large-diameter thin-walled CP-Ti tube. Int. J. Adv. Manuf. Technol. 72, 1187–1203. https://doi.org/10.1007/s00170-014-5709-7

Zhang, Z.Y., Yang, H., Li, H., Ren, N., Wang, D., 2013. Quasi-static tensile behavior and constitutive modeling of large diameter thin-walled commercial pure titanium tube. Mater. Sci. Eng. A 569, 96–105. https://doi.org/10.1016/j.msea.2013.01.055

Zhou, G., Jain, M.K., Wu, P., Shao, Y., Li, D., Peng, Y., 2016. Experiment and crystal plasticity analysis on plastic deformation of AZ31B Mg alloy sheet under intermediate temperatures: How deformation mechanisms evolve. Int. J. Plast. 79, 19–47. https://doi.org/10.1016/j.ijplas.2015.12.006